

To be published in the Astrophysical Journal

The Ionization of Nearby Interstellar Gas

Jonathan D. Slavin¹

Eureka Scientific Inc., 2452 Delmer St. Suite 100, Oakland, CA 94602-3017

and

Priscilla C. Frisch

*University of Chicago, Department of Astronomy and Astrophysics, 5460 S. Ellis Avenue,
Chicago, IL 60637*

ABSTRACT

We present new calculations of the photoionization of interstellar matter within ~ 5 pc of the Sun (which we refer to as the Complex of Local Interstellar Clouds or CLIC) by directly observed radiation sources including nearby hot stars and the diffuse emission of the Soft X-ray Background (SXRb). In addition, we model the important, unobserved EUV emission both from the hot gas responsible for the SXRb and from a possible evaporative boundary between the CLIC and the hot gas. We carry out radiative transfer calculations and show that these radiation sources can provide the ionization and heating of the cloud required to match a variety of observations. The ionization predicted in our models shows good agreement with pickup ion results, interstellar absorption line data towards ϵ CMa, and EUV opacity measurements of nearby white dwarf stars. Including the radiation from the conductive boundary improves agreement with data on the temperature and electron density in the cloud. The presence of dust in the cloud, or at least depleted abundances, is necessary to maintain the heating/cooling balance and reach the observed temperature. Using the column density observations as inputs, we derive the gas phase abundances of C, N, O, Mg, Si, S and Fe. Based on these inferred depletions, it appears that silicate and iron dust exists in the CLIC, while carbonaceous dust has been destroyed.

Subject headings: ISM: clouds — ISM: abundances — ultraviolet: ISM — X-rays: diffuse background – solar system: general — ISM: cosmic rays

¹Also: Harvard-Smithsonian Center for Astrophysics, 60 Garden Street, MS 34, Cambridge, MA 02138

1. Introduction

The study of the interstellar medium (ISM) around and within the Solar System presents us with an unparalleled opportunity to gain understanding of the equilibrium and abundances in warm interstellar gas. Interstellar neutrals, which are able to pass through the boundary between the solar wind and the interstellar medium, constitute $\sim 98\%$ of the diffuse gas within the heliosphere (the solar wind bubble), and form the parent population of the pickup ions (PUI) and anomalous cosmic rays (ACR) seen within the heliosphere. The PUI and ACR provide a direct sample of interstellar gas in the low density cloud that surrounds the Solar System. In turn, the interstellar gas flowing past the Solar System determines the boundary conditions of the heliosphere. By combining observations within the Solar System and towards nearby stars with a theoretical understanding of the processes at work in the local ISM, we can make progress in understanding both the warm interstellar medium and the heliosphere.

The initial discovery of solar Ly α radiation fluorescing off of neutral interstellar hydrogen within the solar system showed that the Sun is immersed in warm tenuous neutral interstellar gas flowing through the solar system at $\sim 25 \text{ km s}^{-1}$ (although solar cycle variations in the radiation pressure on the inflowing atoms produce uncertainties in fixing the cloud velocity Thomas & Krassa 1971; Bertaux & Blamont 1971; Adams & Frisch 1977). Extreme ultraviolet (EUV) observations of the backscattered He 0 584 Å line provided additional insight into the velocity and temperature of ISM within the solar system, without radiation pressure uncertainties (Weller & Meier 1974). More recent data show that the source population of the pickup ions (e.g., Gloeckler 1996) and anomalous cosmic rays (e.g., Cummings & Stone 1996) is composed of interstellar neutrals that enter the heliosphere, are ionized by either charge-exchange with the solar wind or photoionization, and subsequently accelerated (e.g., Fisk et al. 1974). One of the purposes of this study is to determine ionization levels for the interstellar gas at the entry point of these neutrals into the heliosphere.

The overall characteristics of the nearest interstellar gas were determined by the *Copernicus* and IUE satellites. Direct spectroscopic observations by *Copernicus* confirmed that the velocity of interstellar gas inside and outside of the solar system is similar (Adams & Frisch 1977; Landsman et al. 1984). *Copernicus*, IUE and HST observations of nearby stars show that average space densities in local interstellar matter (ISM) are relatively low ($\sim 0.1 \text{ cm}^{-3}$, e.g., McClintock et al. 1975; Bruhweiler & Kondo 1982; Frisch & York 1983), that the gas is relatively warm ($\sim 7000 \text{ K}$, e.g., Landsman et al. 1984, 1986; Murthy et al. 1987; Linsky 1996; Lallement 1996) and that gas-phase abundances of refractory elements are enhanced relative to cold cloud abundances indicating shock destruction of dust grains (Frisch 1981; Frisch et al. 1999).

Both optical and UV data show that even the nearest stars have multiple foreground interstellar clouds, such as $\alpha \text{ Cen}$ ($d = 1.3 \text{ pc}$, two absorption components, Landsman et al. 1984), $\alpha \text{ Aql}$ ($d = 5 \text{ pc}$, three components, Ferlet et al. 1986), and $\alpha \text{ CMa}$ (a.k.a. Sirius, $d = 2.7 \text{ pc}$, two components, Lallement et al. 1994). The velocity of the cloud immediately surrounding the Solar System is

established by *Ulysses* observations of interstellar He^0 (25 km s⁻¹, heliocentric velocity, Witte et al. 1996). Absorption features at this velocity are identified in many nearby stars (e.g., Bertin et al. 1993), but puzzlingly not the nearest star α Cen (Landsman et al. 1984; Linsky & Wood 1996). Nearby interstellar gas at the velocity of heliospheric interstellar He^0 is referred to as the Local Interstellar Cloud (LIC). The two absorption components present towards α CMa are at heliocentric velocities of 12 and 18 km s⁻¹ (Lallement et al. 1994; Hébrard et al. 1999). The 18 km s⁻¹ component corresponds to the LIC vector projected in this direction, and the blue-shifted cloud (BC) velocity corresponds to a cloud at rest in the local standard of rest (for the LSR determined from *Hipparcos* data of 13.4 km s⁻¹ towards galactic coordinates $\ell = 28^\circ$, $b = +32^\circ$, Dehnen & Binney 1998). Given the extremely small distance to the BC component and the relatively small velocity separation between the LIC and BC (less than the LIC sound speed ~ 10 km s⁻¹), we believe these clouds to be physically adjacent. We refer to the complex of interstellar velocity components near the Sun, including the LIC and BC components, as the Complex of Local Interstellar Clouds (CLIC, in place of the term Local Fluff used by Frisch 1995). In this paper specifically, we denote the combined LIC and BC as the CLIC.

The very local ISM offers clues to understanding the ISM in general since the temperature and density of the CLIC are similar to that of the warm ionized medium (WIM). The WIM is a major constituent of the interstellar medium, taking up $\gtrsim 20\%$ of its volume and as much as 1/3 of its mass. Much of our knowledge of the state of the WIM comes from observations of diffuse $\text{H}\alpha$ emission, diffuse emission from other optical lines including [S II] $\lambda 6717$, [N II] $\lambda 6584$, [O III] $\lambda 5007$, and [O I] $\lambda 6300$ (Haffner et al. 1999) and pulsar dispersion measures (e.g., Kulkarni & Heiles 1987). These observations all involve integrations over long pathlengths and therefore smooth out local variations in WIM properties. The ionization of the WIM inferred from such observations is considerably different from the CLIC. [O I] $\lambda 6300$ Å observations have been used to infer that the WIM (in the limited regions for which the line has been observed) is highly ionized, $X_{\text{H}} > 0.67$ (Reynolds 1989). In addition, observations of He I $\lambda 5876$ Å have been used to infer that helium is substantially *less* ionized than hydrogen in the WIM, $X_{\text{He}} \lesssim 0.27 X_{\text{H}}$ (Reynolds & Tufte 1995), though again the observations have been limited to a few locations near the galactic plane.

Pickup ion and absorption line data both indicate that the CLIC has only a moderate ionization level (e.g. $X_{\text{H}} \approx 0.3$) and observations with *EUVE* have shown He to be *more* ionized than H (Dupuis et al. 1995). H I 21 cm observations show widespread non-absorbing warm neutral gas with temperatures generally in the range of 5000–8000 K (e.g., Payne et al. 1983; Kulkarni & Heiles 1988). This warm neutral medium (WNM) is perhaps a better model for the CLIC, though it is generally assumed that H is entirely neutral in such regions. Heiles (2001), however, has shown that $\sim 60\%$ of H I has $T > 500$ K, with $\sim 47\%$ of this gas at temperatures considered thermally unstable ($T = 500 - 5000$ K). Low column density and low velocity warm clouds ($\log N(\text{H I}) < 19$ cm⁻²) are difficult to resolve where cold gas is present, but are common in intermediate and high velocity halo gas (e.g. towards HD 93521, Spitzer & Fitzpatrick 1993).

Generally, low emission measure (< 1 cm⁻⁶ pc) H II gas occurs both as ionized layers on neutral

clouds (Reynolds et al. 1995) and isolated low column density ionized filaments (Haffner et al. 1998). The WIM may represent a collection of regions with a range of ionization characteristics, since H- and He-ionizing radiation is attenuated by an order of magnitude for clouds with $\log N(\text{H}^0) \approx 17.6$ and $\approx 18.1 \text{ cm}^{-2}$, respectively. The hardness of the radiation field thus will vary considerably between clouds with low neutral column densities ($\log N(\text{H}^0) < 18 \text{ cm}^{-2}$). Alternatively, the CLIC may be characteristic of warm, ionized clouds in regions with little to no O star radiation that are ionized primarily by radiation from hot gas.

The ionization of nearby interstellar matter has been inferred from data on Mg^0/Mg^+ (Bruhweiler et al. 1984; Frisch et al. 1990; Lallement et al. 1994) the fine-structure excited states of C^{+*} (York 1983; Wood & Linsky 1997; Holberg et al. 1999), and observations of H I and He I towards nearby white dwarf stars (e.g., Kimble et al. 1993; Dupuis et al. 1995). Vallergera (1996) used *EUVE* observations of H I and He I column densities combined with the directly measured value for $n(\text{He}^0)$ and showed that both H and He are partially ionized with He most likely more ionized than H. Electron densities have been found from C^{+*}/C^+ and Mg^0/Mg^+ ratios but inconsistencies in the derived values ($\sim 0.11 \text{ cm}^{-3}$ vs. $\sim 0.1\text{--}0.3 \text{ cm}^{-3}$) indicate the CLIC ionization has not been well understood up to this point. Recent studies of Ar^0 abundances suggest that photoionization dominates for nearby low column density gas (based on arguments that the large Ar^0 photoionization cross-section reduces the Ar^0/H^0 ratio below ratios expected for recombining gas, Sofia & Jenkins 1998; Jenkins et al. 2000).

There is no single, clearly dominant source for the ionization of the CLIC. The directly observed sources of hydrogen ionizing radiation fall into two categories: stellar EUV sources and diffuse soft X-ray background emission (SXRb). The former have all been observed by *EUVE* and the combined spectrum from the brightest sources has been presented by Vallergera (1998). The most important part of the SXRb for ionization of the CLIC is the low energy Be ($\sim 100 \text{ eV}$) and B band ($\sim 175 \text{ eV}$) radiation which has been observed by the Wisconsin Group using rocket-borne proportional counters. Vallergera (1998) has shown that the stellar EUV sources are not capable of providing the observed He ionization levels (27–50%). We show below that by including the flux from the SXRb, modeled as emission from a $T \sim 10^6 \text{ K}$ collisional ionization equilibrium plasma, we *can* account for the observed ionization. We also show that better agreement with the observations can be achieved if we include the radiation from an evaporative interface at the boundary of the cloud.

Slavin (1989, hereafter S89) explored ionization of the Local Cloud due to ionizing radiation from the boundary of the cloud. In S89 the detailed temperature-density-ionization profiles at the interface of the cloud and the hot gas of the Local Bubble were calculated assuming that conduction was more or less inhibited by the magnetic field. We have improved on the calculations in S89 in several ways. First we treat the radiative transfer in the cloud much more carefully, utilizing the photoionization code CLOUDY (Ferland 1996) for this purpose. In addition we use improved atomic data and codes in our calculations of the radiation generated in the boundary and the resultant ionization. Since this study uses the ionization code CLOUDY to perform the detailed radiative transfer calculation, our models do not make the usual assumption that the cloud

is uniformly ionized, allowing the ionization at the solar location to be distinguished from values derived from absorption line data toward nearby stars. Moreover, substantial progress has been made in determining the physical state of the cloud in recent years and the differences in physical parameters from those assumed in S89 make a substantial difference in the ionization calculations.

2. Properties of the Nearby ISM

2.1. The Interstellar Ionizing Radiation Field

The interstellar radiation field (ISRF) is the primary input to any model for the ionization of low column density clouds such as the CLIC. The degree of uncertainty in the intensity of the field varies greatly over the energy range of importance for the ionization of the cloud (~ 7 – 100 eV). Although still quite uncertain, perhaps the best determined part of the spectrum is the far UV (~ 7 – 13.6 eV) that comes primarily from B stars. In our models we have used the far ultraviolet (FUV) fields of Mathis et al. (1983) and Gondhalekar et al. (1980).

The diffuse soft X-ray background (SXRb, 0.1 – 1 keV) is also very important to cloud ionization, and has been observed over the entire sky by the Wisconsin Group using sounding rockets (McCammon et al. 1983) and with the *ROSAT* satellite (Snowden et al. 1997). The limited energy resolution of the soft X-ray observations does not allow tight constraints to be placed on the emission production mechanism for the SXRb, although thermal emission from a hot plasma appears most likely. Observations by different instruments have found consistent results for the flux within the various energy bands. Thus using the broad band count rates to fix the intensity (i.e. the emission measure, see below) in our model radiation field encourages confidence that interstellar photoionization rates due to soft X-rays are fairly accurate. Since the radiation from an optically thin hot plasma is dominated by line emission, however, we need to keep in mind that a coincidence of an emission line and an absorption edge can still cause substantial differences in photoionization rates calculated for spectra that produce the same band fluxes. Of more importance, however, is the extension of the hot gas emission spectrum down to the EUV energies (i.e. 13.6 – 100 eV) where most of the ionization of elements with first ionization potentials of 13.6 eV and higher occurs. The chemically abundant atoms of He (first ionization potential, FIP= 24.6 eV) and Ne (FIP= 21.6 eV) which are found in the PUI population, and Ar (FIP= 15.84 eV) which is observed both in the ACR population and in absorption in the ISM, are sensitive to EUV fluxes.

The EUV radiation field has important contributions both from the stellar flux from white dwarfs and early type stars, and diffuse emission from plasma interior to the Local Bubble. Observations carried out with *EUVIE* during the all-sky survey have determined flux from all of the brightest stellar EUV sources (Vallerga 1998). The stellar flux (504 – 912 Å) is dominated by emission from two B stars, ϵ CMa and β CMa. The diffuse EUV emission has been searched for but has not been clearly detected to date (see, e.g. Jelinsky et al. 1995; Vallerga & Slavin 1998), though the observation is difficult and no instrument optimized for observations of diffuse emission in the EUV

has yet been flown. In this paper we take the simple approach of using the SXR observations to set the parameters of the Local Hot Bubble plasma model (emission measure, $\int n_e n_{H^+} ds$, and temperature) and then use the emission spectrum predicted by the model at lower (EUV) energies. We discuss some of the uncertainties inherent in this approach below. An uncertain, yet possibly dominant, source of EUV emission is the radiation generated within the interface boundary between the CLIC and Local Bubble plasma as discussed below.

2.2. *In Situ* Observations of the ISM

The most direct observations of nearby interstellar material are observations of interstellar gas and dust within the heliosphere, yielding cloud temperature and space densities of abundant elements. The direct detection of He^0 by *Ulysses* yields $n(\text{He I}) = 0.017 \pm 0.002 \text{ cm}^{-3}$ and a cloud temperature of $T = 7000 \pm 600 \text{ K}$ (Witte et al. 1996). The temperature of He^0 determined from observations of He I 584 Å backscattered radiation, $T = 6900 \pm 600 \text{ K}$, is consistent with this result (Flynn et al. 1998). Although extensive data on interstellar H I in the solar system exist, based on Ly α backscattered radiation (e.g., Chassefiere et al. 1986), somewhat uncertain ionization and radiation pressure corrections and heliopause filtration render these data less reliable for determining the properties of the parent interstellar neutrals. *In situ* data on neutrals in the solar system are listed in Table 1.

Ulysses observed He, Ne, N, and O pickup ions at distances $\sim 2\text{--}5 \text{ AU}$ from the Sun (Gloeckler & Geiss 2001). These data are corrected for ionization and propagation in the solar system, yielding the space densities of interstellar He^0 , Ne^0 , N^0 and O^0 at the termination shock of the solar wind. These values are listed in Table 1. However, up to 30% of interstellar O^0 is lost during transition of the heliopause region by charge exchange which couples interstellar O^0 to the interstellar proton flow deflected around the heliosphere by Lorentz forces (Fahr & Ripken 1984; Izmodenov et al. 1997). In pickup ions, $\text{O}^0/\text{N}^0 \sim 7.0$, compared to the solar abundance ratio $\text{O}/\text{N} \sim 7.9$ (Table 1).

The LIC contains interstellar dust, which has been directly observed by detectors on both the *Ulysses* and *Galileo* satellites (Gruen et al. 1994). The dust grain size distribution and gas-to-dust mass ratios (R_{gd}) determined from these data are problematic for current dust models, with *in situ* data yielding $R_{\text{gd}} < 140$ from direct detections of interstellar dust grains, and $R_{\text{gd}} \sim 425\text{--}550$ from missing-mass arguments applied to absorption line data (depending on assumed reference abundances, Frisch et al. 1999). The upper limit on R_{gd} determined from direct observations applies because small dust grains are deflected around the heliosphere by Lorentz forces. We find below that the actual dust content of the cloud is not of great importance for the heating/cooling balance since dust photoelectric heating is a minor contributor ($\sim 2\%$) to the total heating rate. (In contrast, the gas phase abundances of the most abundant elements do have an important impact on the cooling in the gas.) The fraction of the abundant elements tied up in dust provides important information on the nature of the dust in the LIC and, by extension, in the WIM/WNM in general.

2.3. Absorption Line Data

Line of sight data, i.e. ion column densities, derived from observations of nearby stars provide further constraints on our models of CLIC ionization. HST high resolution (GHRS or STIS) or FUSE data exist for nearby A stars (e.g. α CMa, Hébrard et al. 1999), several cool stars (e.g., Linsky et al. 1995), and white dwarf stars (e.g., Lemoine et al. 1996; Holberg et al. 1999; Jenkins et al. 2000). A fairly complete data set on the CLIC, is found for ϵ CMa (B2 Iab, $\ell, b = 239.8^\circ, -11.3^\circ$, $d = 132$ pc, Gry & Jenkins 2001, hereafter GJ). The stars ϵ CMa and α CMa (A1 V, $\ell, b = 227.2^\circ, -8.9^\circ$, $d = 2.6$ pc) are separated by $\sim 13^\circ$, and ϵ CMa is located in the third-quadrant void (e.g., Frisch & York 1983). The neutral gas observed towards ϵ CMa and α CMa shows the same velocity structure, with the LIC component at ~ 17 km s $^{-1}$, and a second blue-shifted cloud (BC) at ~ 10 km s $^{-1}$ (heliocentric velocities). These data indicate the LIC and BC are both close to the Sun, and we choose to compare our model results with observations of ϵ CMa where data are more complete. Additional ionized gas towards ϵ CMa appears to be more distant, contributing little to neutral abundances (GJ). $N(\text{H I})$ is difficult to determine for low column density sightlines because of saturation in the Ly- α line. Values determined for the total $N(\text{H I})$ towards ϵ CMa include $\log N(\text{H}^0) = 17.98 \pm 0.1$ cm $^{-2}$ (EUVE data, Cassinelli et al. 1995), and $\log N(\text{H}^0) = 17.53\text{--}17.91$ cm $^{-2}$ from various abundance arguments applied to observed column densities (GJ).

The gas phase abundances of elements such as C, N, Mg and Fe in local gas can not be determined directly from observations because while they are formed in both neutral and ionized gas, there is no direct measure of $N(\text{H}^+)$ in the CLIC. Previous studies of the CLIC show that it is neither nearly completely ionized nor completely neutral, but is partially ionized with a significant gradient in the ionization of the cloud from center to edge (e.g., Cheng & Bruhweiler 1990; Vallerga 1996; Slavin & Frisch 1998). Most importantly we do not have any direct measurement of the degree of ionization of hydrogen, although ionization equilibrium estimates using total line column densities for Mg^+ , Mg^0 , C^+ , and C^{++} provide approximate values. Because of these uncertainties, our model treats the gas phase abundances of C, N, O, Mg, Si, S and Fe as parameters which are varied to match observed column densities. Because of its proximity and the quality of the observational data, we use column densities towards ϵ CMa as determined by GJ for this modeling. We include the combined LIC and BC components observed towards ϵ CMa, because both clouds contribute to the attenuation of the dominant ϵ CMa EUV radiation field. Towards ϵ CMa the LIC cloud has $\sim 54\%$ of the neutral gas (GJ), while towards α CMa the LIC has $\sim 40\%$ of the neutral gas (Hébrard et al. 1999). Line width constraints yield a BC temperature of $\sim 3000^{+2000}_{-1000}$ K, and LIC temperature $\sim 8000^{+500}_{-1000}$ K for α CMa. Column densities towards ϵ CMa are given in Table 1. In the modeling process, input abundances are adjusted to force agreement with $N(\text{C II}^*)$, $N(\text{N I})$, $N(\text{O I})$, $N(\text{Mg II})$, $N(\text{Si II})$, $N(\text{S II})$ and $N(\text{Fe II})$. The abundances of C, N, O, Mg, Si, S and Fe therefore can be interpreted as a model result, and compared with our expectations for elemental depletions and undepleted (“reference”) abundances in the local ISM.

We have selected the ϵ CMa sightline for comparison because it is the lowest column density star for which both $N(\text{C II}^*)/N(\text{C II})$ and $N(\text{Mg I})/N(\text{Mg II})$ data are available. Except for the

presence of C IV, which has not yet been detected towards other nearby stars (and has had low upper limits placed on its column density on a few lines of sight, see discussion in §4.1 below), the ϵ CMa sightline is representative of the nearby ISM. For instance, $N(\text{O I})/N(\text{N I}) = 8.3$ and 14.5 for the LIC and BC components, respectively, compared to the range $N(\text{O I})/N(\text{N I}) = 4.0$ –26.3 towards seven nearby white dwarf stars and the two components towards ϵ CMa and α CMa. Nevertheless, as more data becomes available for other lines of sight, it will be important to compare our models with those data sets.

2.4. Magnetic Field

In contrast to the increasingly tight constraints on the temperature and density of the CLIC, the magnetic field strength in the cloud remains poorly determined (Frisch 1990; Ratkiewicz et al. 1998; Gloeckler et al. 1997; Linde 2001). While extremely high fields ($\gtrsim 8\mu\text{G}$) appear to be ruled out due to the lack of detection of the heliospheric bow shock by *Voyager 1*, the range of plausible values for the field still extends from $\sim 1 - 5\mu\text{G}$ (e.g., Gayley et al. 1997; Linde 2001). An argument in favor of the higher end of this range is that the pressure support provided by a field of this strength would help support it against the apparently high thermal pressure of the Local Hot Bubble. Estimates of the bubble pressure based on the observed soft X-ray emission put it at $P/k \sim 10^4\text{ cm}^{-3}\text{ K}$ (Cox & Reynolds 1987; Bowyer et al. 1995). The thermal pressure in our cloud models is more than a third less than that. Nevertheless, the pressure determination for the Local Bubble is indirect and subject to several uncertainties. As a result we explore models with $B = 2\mu\text{G}$ and $5\mu\text{G}$ to span the range of likely values. In one case (model 18), we use $3\mu\text{G}$ in an attempt to find a model that better fit the variety of observational constraints.

3. Photoionization Model

3.1. Radiation from an Evaporative Boundary

If the Local Bubble gas is hot, $T \approx 10^6\text{ K}$, as inferred from the soft X-ray background observations, then a sharp temperature gradient should exist at the boundary between that hot gas and the warm, $T \approx 7000\text{ K}$ LIC gas. In such an interface thermal conduction will cause heat to flow into the cloud and drive an evaporative outflow which produces mass loss from the cloud (see, e.g., Cowie & McKee 1977). (Maximum outflow speeds range from ~ 9 –36 km s^{-1} in our runs and depend strongly on the temperature of the hot gas and weakly on the density of the cloud.) An important consequence is that the cloud gas which is heated, ionized and accelerated outwards will radiate strongly in the EUV.

Emission from the evaporative boundary is modeled using interface models similar to those of S89. The code has been updated and improved, but all the input physics is the same. We assume

steady flow evaporation and spherical symmetry and include the effects of radiative cooling, non-equilibrium ionization and saturation of heat flux. The spectra (as well as necessary ionization, recombination and cooling rates) are calculated using the Raymond & Smith plasma emission code (Raymond & Smith 1977, and updates).

The parameters that need to be specified for the evaporative interface models include the cloud density, n_{cl} (total density including H and He in all ionization states), cloud radius, R_{cl} , temperature of the hot gas, T_h (i.e. the temperature reached at some large r – we choose 30 pc – from the center of the cloud, effectively the temperature of the hot Local Bubble), and cloud magnetic field strength, B_0 . In addition we specify a conductivity reduction factor, η , which reduces the thermal conductivity of the gas in the way that would occur if the mean field direction were at some angle θ relative to the temperature gradient, where $\eta = \cos^2(\theta)$. We have chosen to always set $\eta = 0.5$ (corresponding to $\theta = 45^\circ$) which is the mean value for a field that could be at any random angle to the radial direction. Note that this is different than assuming a randomly tangled field which would result in sharply reduced conductivity. The external ionizing radiation field also affects the cloud evaporation rate due to the effects of ionization, particularly of H and He, on the radiative cooling within the outflow. In a steady flow, the heat flowing into the cloud via thermal conduction is balanced by the radiative cooling in the interface and the enthalpy flux out of the cloud. Thus we also need to specify parameters that influence the radiation field such as the total H I column density and the abundances of the most important elements.

In all the cloud evaporation models presented below we have used $R_{cl} = 3$ pc and $\eta = 0.5$. The interface models have been run for values $n_{cl} = 0.3, 0.33$ and 0.35 ; $B_0 = 2$ and $5 \mu\text{G}$ (except for model 18 which uses $B_0 = 3 \mu\text{G}$) and $T_h = 10^6$ and $10^{6.1}$ K. In addition, we have looked at the effects of varying the cloud column density, $N(\text{H I})$. This is allowed because $N(\text{H I})$ is difficult to measure directly towards the B2 Ia star ϵ CMa and because *EUVE* observations determine the total column density towards the star while we are only interested in the contribution from the CLIC. That is, the *EUVE* lines of sight could be, and in many cases surely are, sampling clouds which do not attenuate the local radiation field. We have evaluated models with $N(\text{H I}) = 4 \times 10^{17}$, 6.5×10^{17} and $9 \times 10^{17} \text{ cm}^{-2}$. *EUVE* data gives total $N(\text{H I}) = 9.5 \pm 2.5 \times 10^{17} \text{ cm}^{-2}$ towards ϵ CMa (Vallerga 1996), while GJ infer $N(\text{H I}) = 3.4 - 8.25 \times 10^{17} \text{ cm}^{-2}$ from abundance arguments. Our choice of $N(\text{H I})$ affects the degree to which the hot gas and interface emission is absorbed between the edge of the CLIC and the Sun but does not affect the stellar EUV emission received at the Sun. This is because we start with the observed flux and “de-absorb” by the amount appropriate to our assumed column density for the CLIC to get the flux incident on the cloud face. The EUV flux incident at the cloud surface thus *does* depend on the assumed value for $N(\text{H I})$, with higher fluxes corresponding to larger $N(\text{H I})$ values. Twenty-five models have been created using these ranges of input variables, and the parameter values for each individual run are listed in Table 2. Included in these are seven models (nos. 19–25) in which it is assumed that the cloud boundary is not conductive so that there is no evaporation at the interface. In this way we are able to test the need for the radiation from an evaporative interface in order to ionize the cloud.

3.2. The Combined Radiation Field and Radiative Transfer

To construct the total radiation field we take the cloud boundary spectrum we have generated from the interface model and combine it with the de-absorbed stellar EUV spectrum, the de-absorbed soft X-ray emission from hot gas and the FUV field of either Mathis et al. (1983) or Gondhalekar et al. (1980). The emission from the hot gas is generated under the assumption of collisional ionization equilibrium of an optically thin plasma using the Raymond & Smith (1977, plus updates) plasma emission code. The total soft X-ray emission (including both the cloud boundary emission and diffuse emission from the Local Bubble) is scaled so as to give us the observed count rate in the Wisconsin B band (~ 175 eV). We choose to peg our flux to these observations since the B band is the softest X-ray band for which there are observations that cover the entire sky. We have also examined cases in which we assume no evaporation of the cloud so that all the soft X-ray emission comes from the hot gas of the Local Bubble. As we discuss below, our ionization models produce a worse match to the observations for the no-interface cases. We alter the diffuse part of the flux somewhat to simulate, in a crude way, the radiative transfer effect of having the diffuse emission coming from the entire sky. This is done by multiplying the flux (effectively the intensity integrated over the sky, $4\pi J_\nu$) by $(1 + (1 - \exp(-2\tau_\nu))/2\tau_\nu)/2$, where τ is the optical depth (center to edge) of the cloud. This expression is exact at the edge of a spherical, constant optical depth cloud subject to a uniform diffuse radiation field.

We show in Figure 1 an example of a radiation field constructed for one of our models (no. 17, one of our preferred models discussed below). In table 3 we list several measures of the radiation field that characterize its hardness and intensity. In the table, U is the ionization parameter, defined as the ratio of the ionizing photon density to total (neutral+ionized) hydrogen density. The quantities ϕ_H , ϕ_{He^0} , and ϕ_{He^+} , are the total ionizing photon fluxes at the cloud surface in photons $\text{cm}^{-2} \text{s}^{-1}$ in three different bands: 13.6–24.6 eV, 24.6–54.4 eV, and 54.4–100 eV respectively. $Q(\text{H}^0)/Q(\text{He}^0)$ is the ratio of the total number of H and He^0 ionizing photons in the incident radiation field. $\langle E \rangle$ is the mean energy (in eV) of an ionizing photon calculated as $\langle E \rangle = \int F_\nu d\nu / \int \frac{F_\nu}{h\nu} d\nu$ where F_ν is the incident energy flux ($\text{ergs cm}^{-2} \text{s}^{-1} \text{Hz}^{-1}$) and the integration limits are from 13.6 eV to 100 eV.

The spectrum of the emission from the hot gas and the cloud boundary is dominated by lines and as a result, the best test of the model would be observations of emission lines generated in the cloud boundary. Up to now no instrument has been had the sensitivity and spectral resolution in the EUV to make such observations possible. The upcoming CHIPS (Cosmic Hot Interstellar Plasma Spectrometer) mission, however, will have the capability to detect and resolve line emission from the cloud boundary. In the CHIPS band (90Å–260Å) the primary emission lines from the boundary are the He II lines at 256Å, 243Å and 237Å in order of decreasing strength. The strengths of these lines correlate strongly with pressure in the hot gas (or total pressure, magnetic + thermal in the cloud gas) and weakly anti-correlate with H I column density. There is also a significant, but non-linear correlation with temperature of the hot gas. For the purposes of predicting the observations, the following rough relationship holds for our models: $I(\text{He II } 256\text{Å}) \approx P/k_B 0.006$

photons $\text{cm}^{-2} \text{ s}^{-1} \text{ sr}^{-1}$. Here the pressure, P/k_B in $\text{cm}^{-3} \text{ K}$, is the thermal pressure in the hot gas or the total pressure in the cloud. The 243Å line is roughly a factor of 3 lower than the 256Å line and the 237Å line is a factor of 3.8 down. Thus for $P/k_B = 10^4 \text{ cm}^{-3} \text{ K}$, the 256Å line is 60 photons $\text{cm}^{-2} \text{ s}^{-1} \text{ sr}^{-1}$, the 243Å line is about 20 and the 237 line is about 16. These intensities are all high enough to be observable with CHIPS. Other lines in the CHIPS band should give us insights into the nature of the bulk hot gas, but the helium lines stand out as indicators of an evaporative cloud boundary.

We have employed the radiative transfer/thermal equilibrium code CLOUDY (version 90.05, Ferland 1996) in the mode in which plane-parallel geometry is assumed. CLOUDY calculates the detailed radiative transfer, including absorption and scattering, of the incident field and the diffuse continuum and emission lines generated within the cloud. Several options may be selected when using the CLOUDY code. We have used commands to include cosmic ray ionization (at the default background level), to assume constant pressure and to include grains but at a 50% abundance (command: grains 0.5). Temperature and ionization are calculated at each point within the cloud. We have used the ionization at the end point, coinciding with the $N(\text{H I})$ value appropriate to our assumption for the generation of the radiation field, to predict the cloud ionization at the heliosphere boundary.

4. Model Results

A range of assumptions were used in our modeling of the CLIC. The parameters of the models are listed in Table 2, and model results presented in Tables 4 and 8, and Figures 2 and 5.

4.1. Column Densities and Abundances

In order to constrain our models and to derive information on the gas phase elemental abundances in the CLIC we use HST observations of nearby interstellar gas towards ϵ CMa, which is similar to the ISM towards α CMa (§2.3). As discussed above, we choose to use the combined LIC and BC column densities for comparison. The model was forced to produce agreement with the observed column densities of $N(\text{C II}^*)$, $N(\text{N I})$, $N(\text{O I})$, $N(\text{Mg II})$, $N(\text{Si II})$, $N(\text{S II})$ and $N(\text{Fe II})$ (Table 1) by adjusting input elemental abundances to the model. Model predictions were then compared with $N(\text{Mg II})/N(\text{Mg I})$ and $N(\text{C II})/N(\text{C II}^*)$, along with data from PUI and He^0 within the solar system (Table 1). (Note: we list the Ulysses value for $n(\text{He I})$ (Witte et al. 1996) in Table 1, while PUI data yield a somewhat lower value, $n(\text{He I}) = 0.0153 \pm 0.002 \text{ cm}^{-3}$. (Gloeckler & Geiss 2001)) The abundances of Mg^0 and C^{+*} are sensitive to electron densities, via radiative and dielectronic recombination for Mg^0 , and collisional excitation of the fine-structure lines for C^{+*} . The ratios $N(\text{Mg II})/N(\text{Mg I})$ and $N(\text{C II})/N(\text{C II}^*)$ provide good tests of our models over spatial scales comparable to the cloud length. Ratios of $N(\text{H I})/N(\text{He I})$ towards nearby white dwarf stars

also provide good tests for the model predictions, however large variations in this ratio are seen locally (e.g. Dupuis et al. 1995; Vallerga 1996; Wolff et al. 1999). Table 4 shows the predicted results for these ratios, as well as $N(\text{H}_{\text{tot}})$, $N(\text{Ar I})$, $N(\text{Ar II})$, and $N(\text{Si III})$. The variations of C^{+*}/C^+ , Mg^0/Mg^+ , n_e and T with depth into the cloud are shown for model no. 17 in Figure 3.

The ratio $N(\text{Mg II})/N(\text{Mg I})$ depends on the electron density, yet it is also sensitive to the strength of the FUV field since the ionization edge of Mg^0 is at $\sim 1622 \text{ \AA}$. Because the fraction of Mg that is neutral, $X(\text{Mg}^0)$, is always very small ($<1\%$), even minor (absolute) changes in the FUV field can alter the ratio $X(\text{Mg}^+)/X(\text{Mg}^0)$ substantially. For this reason two different FUV fields have been explored, using the results of Mathis et al. (1983) and Gondhalekar et al. (1980). The FUV background of Gondhalekar et al. (1980) was based on direct observations of the radiation field with an extrapolation down to 912 \AA done by theoretical calculations of stellar emission and dust scattering and absorption. The intent of Mathis et al. (1983) was to describe the FUV field in a more general way that would apply to the Galaxy at different galactic radii. The differences in the two model backgrounds are not great (with the Mathis et al. (1983) flux somewhat larger than that of Gondhalekar et al. (1980)), yet they are large enough to affect the calculated $N(\text{Mg II})/N(\text{Mg I})$ ratio in our models. As can be seen from comparison of the calculated values of $N(\text{Mg II})/N(\text{Mg I})$ in Table 4 with the observed values in Table 1, in most cases the calculated ratio is larger than the observed ratio. This leads us to favor a lower FUV background flux, closer to that of Gondhalekar et al. (1980). Models 16 and 17 are identical except for the FUV radiation field, which is MMP (16) and GPW (17). The predicted ratios $N(\text{Mg II})/N(\text{Mg I})$ differ by 13% between the models, with Model 17 yielding better agreement with data (346 ± 82 , Table 1).

In contrast to C^{+*}/C^+ , the ratio Mg^0/Mg^+ does not closely follow the electron density. This is clearly illustrated in Figure 3, which shows the predicted variations in n_e , $n(\text{Mg}^0)/n(\text{Mg}^+)$, $n(\text{C}^{+*})/n(\text{C}^+)$, and temperature with depth into the cloud. (Note that the increase of n_e into the cloud is due to a combination of the increased trapping of Lyman continuum recombination radiation and the increase in density in order to maintain the constant pressure.) The difference in the spatial dependence of n_e and Mg^0/Mg^+ is due to the two things: the contribution of charge exchange to the ionization rate of Mg^0 and the temperature dependence of the recombination rate of Mg^+ . Charge exchange ionization of Mg^0 , i.e. via the process $\text{Mg}^0 + \text{H}^+ \rightarrow \text{Mg}^+ + \text{H}^0$, is important for clouds like the CLIC that are warm $T \sim 5000 - 10^4 \text{ K}$ with fairly high electron densities, $n_e \approx 0.1 \text{ cm}^{-3}$. For our case the charge exchange ionization rate coefficient is $\sim 10^{-10} \text{ cm}^3 \text{ s}^{-1}$ at the cloud face as compared with the photoionization rate of $4.7 \times 10^{-11} \text{ s}^{-1}$ for the Gondhalekar et al. (1980) FUV field. The sensitivity to temperature of the recombination coefficient, mostly due to dielectronic recombination in this temperature range, plays the biggest role in breaking the coupling between the electron density and the Mg^0/Mg^+ ratio. For these reasons analyses that find the electron density in clouds using $N(\text{Mg I})/N(\text{Mg II})$ are actually finding an average n_e weighted by the temperature dependence of the Mg^+ recombination coefficient. This is true to some degree even of sophisticated analyses such as carried out by GJ who use both $N(\text{Mg I})/N(\text{Mg II})$ and $N(\text{C II}^*)/N(\text{C II})$ and constrain both n_e and T . An advantage of a radiative transfer calculation

such as we have carried out is that we do not need to assume a constant n_e or T but can simply calculate the integrals directly.

A less ambiguous indicator for electron density is $N(\text{C II}^*)/N(\text{C II})$, which is independent of the radiation field and weakly sensitive to temperature. The rate of excitation to the excited fine structure ($J = 3/2$) level of the ground state of C^+ goes as $\sim T^{0.2}$ for $T \approx 7000$ K (Blum & Pradhan 1992). Moreover cloud temperature is relatively well established (§2.2). Holberg et al. (1999) find $n_e = 0.11^{+0.07}_{-0.06}$ for the LIC from C^+ fine-structure levels towards the white dwarf star REJ 1032+532 ($\ell = 158^\circ$, $b = +53^\circ$, $d = 132$ pc), while Wood & Linsky (1997) find $n_e = 0.11^{+0.12}_{-0.06}$ towards Capella ($\ell = 163^\circ$, $b = +5^\circ$, $d = 12$ pc). These values tend to be smaller than typical electron densities ($0.11\text{--}0.5 \text{ cm}^{-3}$) found towards nearby stars (3–30 pc) from $N(\text{Mg II})/N(\text{Mg I})$ ratios alone (Frisch 1994, 1995; Lallement et al. 1994). GJ determine $n_e = 0.12^{+0.05}_{-0.04}$ for the LIC, and $n_e = 0.052 \pm 0.036$ for the BC, based on mutual constraints imposed by the $N(\text{Mg II})/N(\text{Mg I})$ and $N(\text{C II})/N(\text{C II}^*)$ ratios. The UV data also indicate the BC is evidently cooler than the LIC (3000 vs. 8000 K) (Hébrard et al. 1999). We do not consider these differences in LIC and BC properties here. In future models we will use a more accurate and detailed treatment of the cloud geometry.

We find that the limits on $N(\text{C II})/N(\text{C II}^*)$ (110–280) do not restrict the models very well. High electron densities are achieved for many of the models, though interestingly not for models with no evaporative interface (nos. 19–25). As a result, models with no evaporative interface predict $N(\text{Mg II})/N(\text{Mg I})$ ratios that are factors of 2–3 larger than observed values. The agreement with the observed $N(\text{Mg II})/N(\text{Mg I})$ and $N(\text{C II})/N(\text{C II}^*)$ ratios, along with the predicted temperature and n_{He^0} , cause us to choose our model 17, with $n_e \sim 0.12$ at the Sun, as the “best-fit” model. However, improvements in the uncertainties for column density data may eventually allow better discrimination between the various evaporative interface models. Figure 4 and Figure 5 show the predictions of the models in graphical form. Model no. 18 is in some ways a better model than no. 17 (both are shown as stars in Figures 4 and 5) but produces too high a temperature at the solar location. We discuss this further below.

The column density of $N(\text{Ar I})$ is particularly interesting in that the ionization of Ar is a good discriminant between photoionization equilibrium models and non-equilibrium cooling models in which the local cloud shows the signature of an earlier higher ionization state (Sofia & Jenkins 1998). As Sofia & Jenkins (1998) show, if the Local Cloud had been highly ionized at some earlier epoch, e.g. by a strong shock, and is in the process of recombining, then Ar I and H I will be roughly equally ionized since the recombination coefficients for the ions are nearly the same. The photoionization cross section for Ar I (15.8 eV), is substantially larger than for H I, so if photoionization is dominant, Ar I should be deficient. Jenkins et al. (2000) find a low $N(\text{Ar I})/N(\text{H I})$ ratio for lines of sight that include other gas in addition to the complex of local interstellar clouds, favoring the photoionization equilibrium model over the fossil ionization picture. Our results show a range of values for $N(\text{Ar I})/N(\text{H I})$ though generally showing an even greater ionization of Ar I ($\sim 75\%$) than inferred by Jenkins et al. (2000). Given the relatively large H I column densities, $N(\text{H I}) = 18.36\text{--}18.93 \text{ cm}^{-2}$, observed towards these stars (G191-B2B, GD 394, WD 2211-495, WD 2331-475), a

substantial fraction of the H I and Ar I seen may not be associated with the CLIC.

Also of great interest is the column densities of highly ionized species that are expected to exist in an evaporative cloud boundary. Several studies, motivated by UV observations of absorption lines for long lines of sight through the disk and halo ISM, present calculations of the column densities for C IV, N V, O VI and Si IV in an evaporative boundary (Cowie & McKee 1977; Böhringer & Hartquist 1987; Borkowski et al. 1990). Our results for the models presented in the previous tables are shown in Table 5. These calculations presume a line of sight that is radial in a spherical cloud and passes through only one boundary. Of the high ions listed above only C IV and Si III have been observed towards nearby stars. GJ derive a value for the column density of C IV of $1.2 \pm 0.3 \times 10^{12} \text{ cm}^{-2}$. Our model no. 17 predicts $N(\text{C IV}) \approx 2 \times 10^{12} \text{ cm}^{-2}$, which is about 60% larger than the GJ value. Model no. 18 predicts a value of $N(\text{C IV}) = 1.3 \times 10^{12} \text{ cm}^{-2}$ consistent with GJ’s result. The value of $N(\text{C IV})$ depends on the level of conductivity in the interface (parameter η in the models, see above). Thus model 17 might be brought into agreement with the observations by a small further reduction in η , since a lower conductivity results in less mass loss. If the magnetic field in the cloud is tangled, the conductivity could be reduced by a large factor at all the boundaries of the cloud. The degree to which thermal conductivity is typically suppressed by magnetic field topology in low density interstellar clouds is a difficult and unsolved problem.

We note that Bertin et al. (1995) has put very low upper limits on the C IV column density towards β Leo, β Car and β CMa (4.5×10^{11} , 3.2×10^{11} , and $4.9 \times 10^{11} \text{ cm}^{-2}$, respectively). Thus it would appear that the line of sight towards ϵ CMa has an exceptionally large C IV column density as compared to other nearby lines of sight. Further sensitive searches for C IV and Si IV towards stars within the Local Bubble would help to constrain evaporating cloud models. As we discuss below, the observation of Si III also is problematic for evaporating cloud models. Thus while we have shown that evaporating cloud models do a good job of reproducing the ionization of the cloud, it appears that the boundary surrounding the CLIC is more complex than a steady evaporative flow.

Table 5 gives model predictions for $N(\text{Si III})$, where only the column density formed in the evaporative boundary is listed. The column density in the bulk of the cloud (Table 4) turns out to be of the same order of magnitude as in the boundary for our models. This is a very interesting ion since it is not expected to be abundant in either photoionized gas, which is too cold to produce Si^{++} via collisional ionization, or the cloud boundary gas in which Si is quickly collisionally ionized up to Si^{+3} and beyond. In regions like that in the CLIC in which the radiation field is fairly diffuse, the ionization of Si is controlled by the charge exchange reaction $\text{Si}^{++} + \text{H}^0 \rightleftharpoons \text{Si}^+ + \text{H}^+$. Essentially all the Si is either Si^+ or Si^{++} since Si^0 is ionized by the FUV background. At $T \approx 7000 \text{ K}$, charge exchange results in a very small ionization fraction of Si^{++} , less than 1% in our models. GJ find column densities of $N(\text{Si III}) = 2.3 \pm 0.2 \times 10^{12} \text{ cm}^{-2}$ and $2.0 \pm 1.1 \times 10^{11} \text{ cm}^{-2}$ for the LIC and BC components, respectively. This is far in excess of our calculated values (4×10^9 – 10^{10} cm^{-2}) for this ion. This discrepancy would seem to point to a need for a different type of interface than a classical evaporation front. One possibility that deserves further exploration is that there is a

turbulent mixing layer (see Slavin et al. 1993) at the boundary between the CLIC and the hot gas, at least in some parts of the interface.

The $N(\text{H I})/N(\text{He I})$ ratio observed towards nearby white dwarf star has been one of the more difficult column density ratios to understand. If stellar sources, even very hot stars, are the dominant contributors to the interstellar radiation field, one expects H to be substantially more ionized than He. If He has a 10% abundance, however, the mean observed value of ≈ 14 (Dupuis et al. 1995; Frisch 1995) indicates that He is significantly *more* ionized than H in many sightlines. Photoionization equilibrium thus demands a rather hard spectrum, dominated by diffuse EUV and soft X-ray emission with $E > 24.6$ eV. Alternatively, more distant white dwarf stars (> 50 pc) may sample gas with quite different radiation environments than the CLIC, some of which may be in Stromgren spheres around hot white dwarfs (Wolff et al. 1999; Tat & Terzian 1999). As can be seen from Table 4, our predicted values for $N(\text{H I})/N(\text{He I})$ range between 8.9 and 13.6. Figure 4 shows that this variation is not a simple function of total column density, although higher values of $N(\text{H}_{\text{tot}})$ tend to have smaller $N(\text{H I})/N(\text{He I})$ ratios. This is counter-intuitive, and occurs because the EUV and SXR fluxes are higher at the cloud surface for larger values of $N(\text{H I})$ since the de-absorption factor is greater. Values approaching the observed mean value of 14 result from models with higher temperatures for the hot gas ($\log T_h = 6.1$) in accordance with the need for a relatively hard background spectrum. This result is consistent with the results of Snowden et al. (1998) who find the temperature of the emission from the Local Hot Bubble to be $\log T = 6.07 \pm 0.05$.

The gas phase elemental abundances of C, N, O, Mg, Si and Fe that we derive by combining our model results with the observations are listed in Table 6. The elemental abundances “derived” in the model (found by forcing predicted column densities to match observed column densities, §4.1) are listed in Table 6. Since different models have H I column densities that differ by as much as a factor of 2.25 ($4 \times 10^{17} \text{ cm}^{-2}$ vs. 9×10^{17}), the abundances also vary by more than a factor of 2 between different models. Assuming a small value for $N(\text{H I})$ results in a high value for the abundances. There are some general features of our results, however. O and C have close to the same abundance with O up to 20% higher for some cases. This is in contrast to their solar abundance values (Grevesse 1984) which put the O abundance at $\sim 66\%$ higher than the C value. In addition, there are positive arguments that interstellar abundances may be $\sim 70\%$ of solar abundances, and closer to B-star abundances (Snow & Witt 1996; Savage & Sembach 1996). The predicted values for C for the low $N(\text{H I})$ cases exceed the standard solar abundance value of 490 parts-per-million (ppm), and are well above the standard ISM (i.e. gas phase) value of 140 ppm (Cardelli et al. 1996). The B-star reference abundance for carbon is only 240 ppm further exacerbating the problem. Our results may point to the need for a larger total (gas+dust) C abundance, at least for the very local ISM. This could be related to the larger “carbon crisis” of insufficient carbon to explain both the dust and gas phase abundances of C in the ISM (see Kim & Martin 1996). The derived abundance for O (245–562 ppm) ranges from 31–70% below the solar value indicating O atoms are depleted onto dust. This range encompasses the O abundance found for typical diffuse interstellar clouds (O/H = 319 ± 14 ppm Meyer et al. 1998). The abundance of N also slightly exceeds its solar value

for the high $N(\text{H I})$ cases. Mg, Si and Fe (solar abundances 38, 35 and 47 ppm respectively) on the other hand, are substantially depleted in all cases. Taken at face value, these results would indicate that graphite or other carbonaceous grains have been destroyed in the Local Cloud, but that silicate and iron grains have survived.

4.2. Comparisons with Heliospheric ISM Data

A novel aspect of this study is that we can compare model predictions with *in situ* observations of interstellar atoms within the solar system (Table 1), including He, N, O, and Ne from pickup ion data (Gloeckler & Geiss 2001, hereafter GG), and $n(\text{He}^0)$ and T from Ulysses data (Witte et al. 1996). Direct observations of $n(\text{He}^0)$ determined from *in situ* observations of interstellar gas within the solar system provide important constraints on cloud space density (Table 1). Model predictions for the interstellar gas at the heliospheric boundaries are presented in Tables 7 and 8, and Figures 4 and 5. The observed value, $n(\text{He}^0) = 0.017 \text{ cm}^{-3}$, is higher than would be expected if the electron density were low, $n_e \lesssim 0.1 \text{ cm}^{-2}$ consistent with our findings. In addition, if the $N(\text{H I})/N(\text{He I})$ column density ratio for the LIC+BC is close to the average value of 14 (Dupuis et al. 1995), then $n(\text{H}^0) \gtrsim 0.24$, since the ionization of H will decrease into the cloud faster than that of He (e.g., Vallerga 1996). CLOUDY requires an initial input assumption for the total H density (neutral+ionized) at the outer edge of the cloud. The models show that initial total space densities of $n \sim 0.3 \text{ cm}^{-3}$ or more tend to produce a better match with observations of He^0 in the solar system.

One interesting result is that despite large variations in model input parameters, and differences in predicted abundances and other output parameters, the ionization fraction of H at the position of the solar system is found to be relatively constant between the models and within the range $\sim 20\%$ to 30% . The predicted He ionization ranges from $\sim 30\%$ to 50% at the solar location.

The PUI data on O, N, Ne, and He (Gloeckler & Geiss 1998, GG) provide additional constraints on cloud ionization. We do not use ACR data (e.g. Cummings & Stone 1996) for comparison (e.g. Frisch 1994), because of the uncertain corrections for propagation and acceleration of ACR's in the heliosphere. Note that to derive the neutral fraction for elements observed in the PUIs, one needs only to use data presented in Tables 6 and 7. For element Z (i.e. O, N or Ne) the neutral fraction is $X(Z^0) = (n(Z^0)/n(\text{He}^0))(n(\text{He}^0)/n(\text{H}^0))(1 - X(\text{H}))/A_Z$ where A_Z is the abundance of Z . Absorption line data towards ϵ CMa yield column density ratios $N(\text{O}^0)/N(\text{N}^0) = 9.7^{+3.0}_{-1.9}$, while PUI data give space density ratios of $n(\text{O}^0)/n(\text{N}^0) = 7.0 \pm 1.5$ at the termination shock (Table 1). Our model predictions for $n(\text{O}^0)/n(\text{N}^0)$ (9.4–10.2 before filtration) are close to the observed ratio from ϵ CMa data (in part because column densities were used to constrain the models). However, up to 20–30% of interstellar O^0 atoms may be ionized while crossing the heliopause region by charge exchange ionization with interstellar protons compressed upstream of the heliopause (e.g. Fahr & Ripken 1984; Izmodenov et al. 1999). Some N^0 ionization may also occur in this region. Both models 17 and 18 require at least $\sim 20\%$ O filtration in the heliopause region to be consistent with

the PUI data (assuming N is unaffected by filtration). The constraint is actually looser than this, however, if we take into account the fairly large uncertainty in the O I column density which was used to set the O abundance in the models.

The variations of the model predictions for $n(\text{O}^0)/n(\text{He}^0)$ (0.004–0.009) are larger than for the PUI O/He. For model 17, which does very well fitting other observational constraints, the $n(\text{O}^0)/n(\text{He}^0)$ ratio, 0.009, is substantially above the PUI value, 0.0037. In this case, an unrealistically large filtration factor ($\sim 50\%$) is required to bring calculated and observed values into agreement. Model 18, however, requires only about 20% O filtration. Model 18 also agrees better with the N/He PUI ratio than model 17, with a predicted $n(\text{N}^0)/n(\text{He}^0)$ ratio (5.9×10^{-4}) within the uncertainties of the PUI value ($5.2 \pm 1.1 \times 10^{-4}$). Other models predict values ranging from $4\text{--}9 \times 10^{-4}$ for this ratio.

Finally, the models predict a value for $n(\text{Ne}^0)/n(\text{He}^0) = 2.5 - 4.2 \times 10^{-4}$, which is smaller than the observed value ($6.0 \pm 1.5 \times 10^{-4}$). We have assumed a Ne abundance of 123 ppm, based on solar abundances. Based on the results of these models, it appears that the Ne abundance in the ISM near the Sun is significantly larger than the “solar” abundance of Ne (which is based on meteoritic measurements). There is some support for larger values for Ne abundances, since 6 out of 7 planetary nebulae show $\text{Ne}/\text{O} = 0.22 - 0.24$, versus the solar value of 0.16 (Howard et al. 1997), suggesting a Ne abundance of ≈ 180 ppm. Based on the relative success of our best models in matching both PUI and absorption line data, and the fact that the ionization potentials of He (24.6 eV) and Ne (21.6 eV) are relatively close, we conclude that the Ne abundance in the cloud around the solar system may be ~ 175 ppm.

In Figure 2 we plot the density of H I, He I, Ne I, O I and N I as a function of depth into the cloud for model 17, one of our “best fit” models. For almost all of the neutral ions, density increases away from the cloud surface because the ionization level decreases. The degree of variation of the densities indicates how the position of the Sun within the cloud and the column density of the cloud can affect neutral ion density ratios derived from the PUI and ACR data. We list in Table 8 the fraction of the element in each ionization stage at the solar location (for model no. 17). Figure 2 demonstrates the tight coupling of O and H ionization by charge exchange (Field & Steigman 1971). The slight decline in $n(\text{H}^0)$ away from the cloud surface seen in the figure (and the increase in n_e seen in Figure 3) is caused by the increased trapping of Lyman continuum flux generated in the cloud by recombination in combination with a decrease in temperature. The increased trapping of Lyman continuum in the cloud interior results in a lower effective recombination coefficient which results in a flat or slightly increasing ionization fraction for H despite the decreasing (due to absorption) photoionization rate. The decrease in temperature results in a higher total density (in order to maintain the constant thermal pressure). Deeper into the cloud, the effective recombination rate approaches its case B value ($3.5 \times 10^{-13} \text{ cm}^3 \text{ s}^{-1}$ at $T = 7000 \text{ K}$) and the temperature flattens out leading to a decrease in n_e and increase in $n(\text{H}^0)$ near the cloud center.

The ionization of N is weakly coupled to H by charge exchange (Butler & Dalgarno 1979).

Both the charge exchange recombination coefficient and the charge exchange ionization coefficient are roughly equal to the radiative recombination coefficient ($\sim 10^{-12} \text{ cm}^3 \text{ s}^{-1}$) at the temperature of the LIC ($\sim 7000 \text{ K}$). The photoionization rate at the cloud face for our model of the radiation field ($\sim 2 \times 10^{-13}$) is such that photoionization exceeds charge exchange ionization by a factor of ~ 2 . Thus, while N ionization is influenced by H ionization, the coupling is not very tight. Photoionization and recombination of free electrons alone would lead to a higher ionization fraction of N, while charge transfer with H alone would lead to lower ionization fraction (roughly equal to that of H). Note that the important role of photoionization in the ionization balance of N gives us an indication of the hardness of the radiation field near $\sim 20 \text{ eV}$ since the photoionization cross section of N is generally larger than that of H, rising from 2.4 times as large at threshold to ~ 19 times at 100 eV .

Observations of nearby white dwarf stars yield a range of values for $N(\text{O I})/N(\text{N I})$, including 4.0 ± 1.4 towards REJ 1032+532 (Holberg et al. 1999, 132 pc, $\log N(\text{H}^0) = 18.62 \text{ cm}^{-2}$), and 7–20 for four white dwarf stars (Jenkins et al. 2000, 50–80 pc, $\log N(\text{H}^0) = 16.73 - 18.25 \text{ cm}^{-2}$). The ratio $N(\text{O I})/N(\text{N I})$ appears highly variable in low column density gas, and may serve as a discriminant between mostly neutral versus partially ionized low density ($N(\text{H I}) \ll 10^{18} \text{ cm}^{-2}$) interstellar clouds.

The temperature of the Local Cloud turns out to be one of the more difficult observations to match. Many models that appear acceptable in other ways predict cloud temperatures that are substantially too high. As we discuss below, this could very well be due to errors and uncertainties in the atomic data used by the codes to calculate our models. Given the difficulties and uncertainties present in thermal equilibrium calculations, we consider it impressive that, without adjustment of parameters for this purpose, we are able to come so close to matching the temperature of the cloud at the solar system. Figure 4 shows the temperature predictions of the different models.

5. Discussion

5.1. Model Assumptions and Reliability

There are a number of assumptions made in our modeling of the Local Cloud that may be questioned. Perhaps foremost of these is the assumption of steady state photoionization equilibrium (see Lyu & Bruhweiler 1996). The H recombination time is $1/(\alpha^{(2)} n_e) \approx 9 \times 10^5 \text{ yr}$, for $n_e = 0.1 \text{ cm}^{-3}$ and $T \approx 7000 \text{ K}$ and it is quite likely that the Local Cloud has experienced at least a moderately fast shock ($v_s \sim 50 \text{ km s}^{-1}$) during that time. The observations of a low $N(\text{Ar I})/N(\text{H I})$ ratio by Jenkins et al. (2000) referred to above favor the interpretation that Ar is primarily photoionized and that non-equilibrium recombination is not the dominant effect in determining the ionization of the cloud. We note in addition that our results show that the local interstellar radiation field is quite capable of providing the moderately high level of ionization that is observed for the CLIC. Any fossil ionization from an energetic event (e.g. the passage of supernova shock) in the relatively

recent past would appear to be insignificant at this point, since the ionization of the cloud does not seem to be in excess of what we expect from the ISRF.

One may also question the reliability and assumptions implicit in our calculations of the radiation field from the hot gas and the evaporative boundary. Plasma emission codes are currently in a state of substantial revision and new and more detailed atomic data are being incorporated into these codes leading to significant changes in predicted spectra. The Raymond & Smith code that we have used to generate the background radiation field is known to be inaccurate in predicting a number of spectral features observed in recent X-ray spectra using, e.g. ASCA and the Chandra X-ray Observatory. These problems are of concern to us, though we feel, for the following reasons, that for our purposes the inaccuracies in the code probably do not strongly affect our results. First, we are concerned only with the photoionization caused by the background flux and not with the strengths of individual emission lines. While individual spectral features could be incorrect, the cross section averaged flux may be fairly accurate. Second, we scale the field strength to be consistent with the observed band rate in the soft X-rays (i.e. the B band), insuring that, at least over the range of the band coverage ($\sim 130 - 188$ eV), the photon flux is not far from the true value. As more observations of the diffuse background, particularly in the EUV, and updated plasma emission codes become generally available, we will be able to revise our background spectrum and reevaluate the ionization rate in the CLIC.

One particularly difficult aspect of the ionization calculation is the treatment of the geometry of radiative transfer. The sources of the background radiation field include: stars, point sources distributed across the sky (but dominated by ϵ CMa and β CMa); the hot gas of the Local Bubble, roughly evenly distributed across the sky and generated from the volume of the Bubble; and interface radiation generated in a thin volume between the warm gas of the cloud and the hot gas of the bubble. Each of these three sources demands a somewhat different radiative transfer technique. In addition the Sun is not at the center of the complex of local interstellar clouds but rather appears to be near the edge (Frisch 1995). Moreover, the Blue Cloud seems to have a lower temperature and somewhat higher density than the LIC (Lallement et al. 1994; Hébrard et al. 1999; Gry & Jenkins 2001). Clearly the full radiative transfer calculation in this situation would be extremely difficult and subject to many uncertainties. Nevertheless, a more complex geometrical model may be warranted as more data on the shape and size of the Local Cloud and the background radiation fields becomes available since these results show the ionization at the solar system depends somewhat sensitively on the ionizing flux recieved at our location within the cloud. In future work we intend to refine our treatment of the radiative transfer in the cloud and explore its effects on the ionization at the solar location and throughout the cloud. In addition we will explore ways to include the differences in LIC and BC properties in our analysis.

6. Conclusions

We have presented results of a calculation of the ionization of the complex of local interstellar clouds (LIC and BC) due to the background interstellar radiation field. The radiation field is constructed from directly observed sources including nearby stellar sources (B stars and white dwarfs) and diffuse emission from the hot gas in the Local Hot Bubble. In addition, emission from a proposed evaporative boundary between the warm cloud and surrounding hot gas is included. Our results show that this radiation field is capable of maintaining the ionization and heating necessary to explain a variety of observations including: column densities of several ions towards ϵ CMa neutral atom ratios derived from PUI data, the temperature of the cloud and the density of He I observed in the solar system.

Our best models for the CLIC show good agreement with $N(\text{Mg I})/N(\text{Mg II})$, $N(\text{C II}^*)/N(\text{C II})$ ratios for the ϵ CMa sightline. The high mean electron density inferred from the ratios $N(\text{C II})/N(\text{C II}^*)$ and $N(\text{Mg II})/N(\text{Mg I})$ towards ϵ CMa requires a local electron density at the Sun, $n_e \approx 0.1 \text{ cm}^{-3}$. This in turn requires a high EUV flux, larger than can be provided by either the stellar EUV flux or the diffuse emission from the hot gas of the Local Bubble. Thus we find evidence for an evaporative boundary to the Local Cloud as an additional source of EUV emission.

One model, no. 17, fits the column density ratio data, and the *in situ* data on T and $n(\text{He}^0)$. The only significant problem for this model is the ratio $n(\text{O}^0)/n(\text{He}^0)$ which is too large compared with the data. Other potential problems for that model include a large required C abundance (427 ppm) a large magnetic field, 5 μG , and a small H I column density, $4 \times 10^{17} \text{ cm}^{-2}$. Models 11 and 18 fit the column density ratio data, and the *in situ* $n(\text{He}^0)$ and the PUI data (with the exception of $n(\text{Ne}^0)/n(\text{He}^0)$, see discussion below). Both models predict the temperature at the Sun to be somewhat too high, however. On the other hand, both models assume lower magnetic fields and higher column densities and predict lower gas phase abundances (e.g., 309 ppm for C for model 18) all of which are to some degree more in keeping with our expectations.

By tying our results to observed column densities for a number of ions towards ϵ CMa, we are able to draw conclusions on the gas phase elemental abundances of those elements Table 4. We find that the gas phase abundances of O, Mg, Si and Fe all show substantial depletion relative to solar abundances. N, S and especially C appear to be undepleted and even to have abundances somewhat above the standard solar values. Taken at face value we would conclude that the LIC/BC complex has a significant amount of silicate and, possibly Fe dust but that the carbonaceous dust has been destroyed. The results show clearly that for most elements both H^0 and H^+ must be included when finding the intrinsic abundance of an element in low column density clouds.

We also find that our models, which are based on a gas phase abundance for Ne of 123 ppm from solar abundances, predict substantially lower values for the ratio $n(\text{Ne}^0)/n(\text{He}^0)$ ($\sim 3 \times 10^{-4}$) at the solar location than is observed for the PUIs ($\sim 6 \times 10^{-4}$). Planetary nebulae data suggest a Ne abundance of ≈ 175 ppm (Howard et al. 1997), which is in better agreement with our models. This comparison suggests that ionization models constrained by pickup ion data

offer unique information on chemical abundances in the ISM, although we can not claim yet that our models provide definitive results. However, the PUI data allow tighter constraints on the models than available from absorption line data alone, and eventually will yield higher standards of accuracy for these models. Future data that would be very helpful would be the determination of $n(\text{Ar}^0)/n(\text{He}^0)$ at the entry point to the heliosphere, either through new PUI data or through the interpretation of existing Ar data in the anomalous cosmic ray population.

The relatively good agreement between predictions of our photoionization model for local interstellar gas and both line-of-sight column densities towards ϵ CMa and *in situ* observations of the ISM products in the solar system strengthens our confidence that radiative transfer codes provide viable models of clouds in space. The radiation in the FUV, EUV and soft X-rays, play a key role in maintaining ionization levels for a range of elements with a range of ionization potentials. Cloud interface emission (or another source with a similar flux in the EUV) evidently must be included for accurate model predictions that match data. By restricting our models to the relatively well known nearby interstellar gas, where we have the special situation that *in situ* observations of the space densities of selected elements are available (including neutrals not seen in absorption), these models must be considered better constrained than previous applications of ionization codes, even though fundamental uncertainties remain.

The physical properties of the interplanetary environment within our solar system, and in extra-solar planetary systems, are governed by the interaction of stellar winds and the ISM (e.g. Frisch 1993). The heliospheric configuration is sensitive to the pressure components of excluded charged particles (Holzer 1989). By combining an ionization model of the ISM with observations of neutral interstellar He, N, O, Ne, and H atoms within the heliosphere we are able to determine interstellar electron density immediately outside of the heliosphere. This photoionization model is especially useful since the ionized component of the ISM can not be measured directly at the solar location, yet provides a critical boundary condition of the heliosphere.

The interstellar cloud surrounding the solar system presents a unique opportunity to determine the physics of a single low density warm interstellar cloud, including both gas and dust components. Low density clouds ($< 10^{18} \text{ cm}^{-2}$) such as the material surrounding the solar system generally are seen only where high cloud velocities resolve weak individual components (e.g. Spitzer & Fitzpatrick 1993; Welty et al. 1999). It is essential that the charged component of this cloud be understood before spacecraft are launched to conduct *in situ* studies of this ISM (e.g. Liewer et al. 2000).

This research was supported by NASA grants NAG 5-5077, NAG 5-6405, and NASW-98027. We have greatly benefitted from helpful discussions with Alan Cummings, George Gloeckler, Dick Mewaldt, Dan Welty, and Gary Zank. PCF would also like to thank Carl Heiles and the Astronomy Department at the University of California, Berkeley, for acting as a host during part of this research. We thank the referee, John Vallergera, for comments that helped to improve this paper significantly.

REFERENCES

- Adams, T. F. & Frisch, P. C. 1977, *ApJ*, 212, 300
- Bertaux, J. L. & Blamont, J. E. 1971, *A&A*, 11, 200
- Bertin, P., Lallement, R., Ferlet, R., & Vidal-Madjar, A. 1993, *J. Geophys. Res.*, 98, 15193
- Bertin, P., Vidal-Madjar, A., Lallement, R., Ferlet, R., & Lemoine, M. 1995, *A&A*, 302, 889
- Blum, R. D. & Pradhan, A. K. 1992, *ApJS*, 80, 425
- Böhringer, H. & Hartquist, T. W. 1987, *MNRAS*, 228, 915
- Borkowski, K. J., Balbus, S. A., & Fristrom, C. C. 1990, *ApJ*, 355, 501
- Bowyer, S., Lieu, R., Sidher, S. D., Lampton, M., & Knude, J. 1995, *Nature*, 375, 212
- Bruhweiler, F. C. & Kondo, Y. 1982, *ApJ*, 259, 232
- Bruhweiler, F. C., Oegerle, W., Weiler, E., Stencel, R. E., & Kondo, Y. 1984, in *Local Interstellar Medium*, 64
- Butler, S. E. & Dalgarno, A. 1979, *ApJ*, 234, 765
- Cardelli, J. A., Meyer, D. M., Jura, M., & Savage, B. D. 1996, *ApJ*, 467, 334
- Cassinelli, J. P., Cohen, D. H., Macfarlane, J. J., Drew, J. E., Lynas-Gray, A. E., Hoare, M. G., Vallergera, J. V., Welsh, B. Y., Vedder, P. W., Hubeny, I., & Lanz, T. 1995, *ApJ*, 438, 932
- Chassefiere, E., Bertaux, J. L., Lallement, R., & Kurt, V. G. 1986, *A&A*, 160, 229
- Cheng, K. & Bruhweiler, F. C. 1990, *ApJ*, 364, 573
- Cowie, L. L. & McKee, C. F. 1977, *ApJ*, 211, 135
- Cox, D. P. & Reynolds, R. J. 1987, *ARA&A*, 25, 303
- Cummings, A. C. & Stone, E. C. 1996, *Space Science Reviews*, 78, 117
- Dehnen, W. & Binney, J. J. 1998, *MNRAS*, 298, 387
- Dupuis, J., Vennes, S., Bowyer, S., Pradhan, A. K., & Thejll, P. 1995, *ApJ*, 455, 574
- Fahr, H. J. & Ripken, H. W. 1984, *A&A*, 139, 551
- Ferland, G. 1996, *Hazy, a Brief Introduction to Cloudy* (University of Kentucky Department of Physics and Astronomy Internal Report)
- Ferlet, R., Vidal-Madjar, A., & Lallement, R. 1986, *A&A*, 163, 204

- Field, G. B. & Steigman, G. 1971, *ApJ*, 166, 59
- Fisk, L. A., Kozlovsky, B., & Ramaty, R. 1974, *ApJ*, 190, L35
- Flynn, B., Vallergera, J., Dalaudier, F., & Gladstone, G. R. 1998, *J. Geophys. Res.*, 103, 6483
- Frisch, P. C. 1981, *Nature*, 293, 377
- . 1990, in *Physics of the Outer Heliosphere*, 19
- . 1993, *ApJ*, 407, 198
- . 1994, *Science*, 265, 1423
- . 1995, *Space Science Reviews*, 72, 499
- Frisch, P. C., Dorschner, J. M., Geiss, J., Greenberg, J. M., Grün, E., Landgraf, M., Hoppe, P., Jones, A. P., Krätschmer, W., Linde, T. J., Morfill, G. E., Reach, W., Slavin, J. D., Svestka, J., Witt, A. N., & Zank, G. P. 1999, *ApJ*, 525, 492
- Frisch, P. C., Welty, D. E., York, D. G., & Fowler, J. R. 1990, *ApJ*, 357, 514
- Frisch, P. C. & York, D. G. 1983, *ApJ*, 271, L59
- Gayley, K. G., Zank, G. P., Pauls, H. L., Frisch, P. C., & Welty, D. E. 1997, *ApJ*, 487, 259
- Gloeckler, G. 1996, *Space Science Reviews*, 78, 335
- Gloeckler, G., Fisk, L. A., & Geiss, J. 1997, *Nature*, 386, 374
- Gloeckler, G. & Geiss, J. 1998, *Space Science Reviews*, 86, 127
- . 2001, *Space Science Reviews*, in press (GG)
- Gondhalekar, P. M., Phillips, A. P., & Wilson, R. 1980, *A&A*, 85, 272
- Grevesse, N. 1984, *Phys. Scr*, 8, 49
- Gruen, E., Gustafson, B., Mann, I., Baguhl, M., Morfill, G. E., Staubach, P., Taylor, A., & Zook, H. A. 1994, *A&A*, 286, 915
- Gry, C. & Dupin, O. 1998, in *Berlin Springer Verlag Lecture Notes in Physics, The Local Bubble and Beyond*, Vol. 506, 161–164
- Gry, C. & Jenkins, E. 2001, *A&A*, 367, 617 (GJ)
- Haffner, L. M., Reynolds, R. J., & Tufte, S. L. 1998, *ApJ*, 501, L83
- . 1999, *ApJ*, 523, 223

- Hébrard, G., Mallouris, C., Ferlet, R., Koester, D., Lemoine, M., Vidal-Madjar, A., & York, D. 1999, *A&A*, 350, 643
- Heiles, C. 2001, *ApJ*, 55, L105
- Holberg, J. B., Bruhweiler, F. C., Barstow, M. A., & Dobbie, P. D. 1999, *ApJ*, 517, 841
- Holzer, T. E. 1989, *ARA&A*, 27, 199
- Howard, J. W., Henry, R. B. C., & McCartney, S. 1997, *MNRAS*, 284, 465
- Izmodenov, V., Malama, Y. G., & Lallement, R. 1997, *A&A*, 317, 193
- Izmodenov, V. V., Geiss, J., Lallement, R., Gloeckler, G., Baranov, V. B., & Malama, Y. G. 1999, *J. Geophys. Res.*, 104, 4731
- Jelinsky, P. J., Vallergera, J. V., & Edelstein, J. 1995, *ApJ*, 442, 653
- Jenkins, E. B., Oegerle, W. R., Gry, C., Vallergera, J., Sembach, K. R., Shelton, R. L., Ferlet, R., Vidal-Madjar, A., York, D. G., Linsky, J. L., Roth, K. C., Dupree, A. K., & Edelstein, J. 2000, *ApJ*, 538, L81
- Kim, S. & Martin, P. G. 1996, *ApJ*, 462, 296
- Kimble, R. A., Davidsen, A. F., Blair, W. P., Bowers, C. W., Dixon, W. V. D., Durrance, S. T., Feldman, P. D., Ferguson, H. C., Henry, R. C., Kriss, G. A., Kruk, J. W., Long, K. S., Moos, H. W., & Vancura, O. 1993, *ApJ*, 404, 663
- Kulkarni, S. R. & Heiles, C. 1987, in *Interstellar Processes*, 87
- Kulkarni, S. R. & Heiles, C. 1988, *Neutral hydrogen and the diffuse interstellar medium (Galactic and Extragalactic Radio Astronomy)*, 95
- Lallement, R. 1996, *SSR*, 78, 361
- Lallement, R., Bertin, P., Ferlet, R., Vidal-Madjar, A., & Bertaux, J. L. 1994, *A&A*, 286, 898
- Landsman, W. B., Henry, R. C., Moos, H. W., & Linsky, J. L. 1984, *ApJ*, 285, 801
- Landsman, W. B., Murthy, J., Henry, R. C., Moos, H. W., Linsky, J. L., & Russell, J. L. 1986, *ApJ*, 303, 791
- Lemoine, M., Vidal-Madjar, A., Bertin, P., Ferlet, R., Gry, C., & Lallement, R. 1996, *A&A*, 308, 601
- Liewer, P. C., Mewaldt, R. A., Ayon, J. A., & Wallace, R. A. 2000, in *Space Technology and Applications International Forum-2000 (AIP CP504)*, ed. M. S. El-Genk, 911
- Linde, T. J. 2001, *Geophys. Res. Lett.*, in press

- Linsky, J. L. 1996, *Space Science Reviews*, 78, 157
- Linsky, J. L., Diplas, A., Wood, B. E., Brown, A., Ayres, T. R., & Savage, B. D. 1995, *ApJ*, 451, 335
- Linsky, J. L. & Wood, B. E. 1996, *ApJ*, 463, 254
- Lyu, C. H. & Bruhweiler, F. C. 1996, *ApJ*, 459, 216
- Mathis, J. S., Mezger, P. G., & Panagia, N. 1983, *A&A*, 128, 212
- McCammon, D., Burrows, D. N., Sanders, W. T., & Kraushaar, W. L. 1983, *ApJ*, 269, 107
- McClintock, W., Henry, R. C., Moos, H. W., & Linsky, J. L. 1975, *ApJ*, 202, 733
- Meyer, D. M., Jura, M., & Cardelli, J. A. 1998, *ApJ*, 493, 222
- Murthy, J., Henry, R. C., Moos, H. W., Landsman, W. B., Linsky, J. L., Vidal-Madjar, A., & Gry, C. 1987, *ApJ*, 315, 675
- Payne, H. E., Salpeter, E. E., & Terzian, Y. 1983, *ApJ*, 272, 540
- Ratkiewicz, R., Barnes, A., Molvik, G. A., Spreiter, J. R., Stahara, S. S., Vinokur, M., & Venkateswaran, S. 1998, *A&A*, 335, 363
- Raymond, J. C. & Smith, B. W. 1977, *ApJS*, 35, 419
- Reynolds, R. J. 1989, *ApJ*, 345, 811
- Reynolds, R. J. & Tufte, S. L. 1995, *ApJ*, 439, L17
- Reynolds, R. J., Tufte, S. L., Kung, D. T., McCullough, P. R., & Heiles, C. 1995, *ApJ*, 448, 715
- Savage, B. D. & Sembach, K. R. 1996, *ARA&A*, 34, 279
- Slavin, J. D. 1989, *ApJ*, 346, 718 (S89)
- Slavin, J. D. & Frisch, P. C. 1998, in *Proceedings of the IAU Colloquium No. 166 “The Local Bubble and Beyond”*, *Lecture Notes in Physics*, Vol. 506, 305
- Slavin, J. D., Shull, J. M., & Begelman, M. C. 1993, *ApJ*, 407, 83
- Snow, T. P. & Witt, A. N. 1996, *ApJ*, 468, L65
- Snowden, S. L., Egger, R., Finkbeiner, D. P., Freyberg, M. J., & Plucinsky, P. P. 1998, *ApJ*, 493, 715
- Snowden, S. L., Egger, R., Freyberg, M. J., McCammon, D., Plucinsky, P. P., Sanders, W. T., Schmitt, J. H. M. M., Truemper, J., & Voges, W. 1997, *ApJ*, 485, 125

- Sofia, U. J. & Jenkins, E. B. 1998, *ApJ*, 499, 951
- Spitzer, L. J. & Fitzpatrick, E. L. 1993, *ApJ*, 409, 299
- Tat, H. H. & Terzian, Y. 1999, *PASP*, 111, 1258
- Thomas, G. E. & Krassa, R. F. 1971, *A&A*, 11, 218
- Vallerga, J. 1996, *Space Science Reviews*, 78, 277
- . 1998, *ApJ*, 497, 921
- Vallerga, J. & Slavin, J. 1998, in *Berlin Springer Verlag Lecture Notes in Physics*, v.506, Vol. 506, 79
- Weller, C. S. & Meier, R. R. 1974, *ApJ*, 193, 471
- Welty, D. E., Hobbs, L. M., Lauroesch, J. T., Morton, D. C., Spitzer, L., & York, D. G. 1999, *ApJS*, 124, 465
- Witte, M., Banaszkiewicz, M., & Rosenbauer, H. 1996, *Space Science Reviews*, 78, 289
- Wolff, B., Koester, D., & Lallement, R. 1999, *A&A*, 346, 969
- Wood, B. E. & Linsky, J. L. 1997, *ApJ*, 474, L39
- York, D. G. 1983, *ApJ*, 264, 172

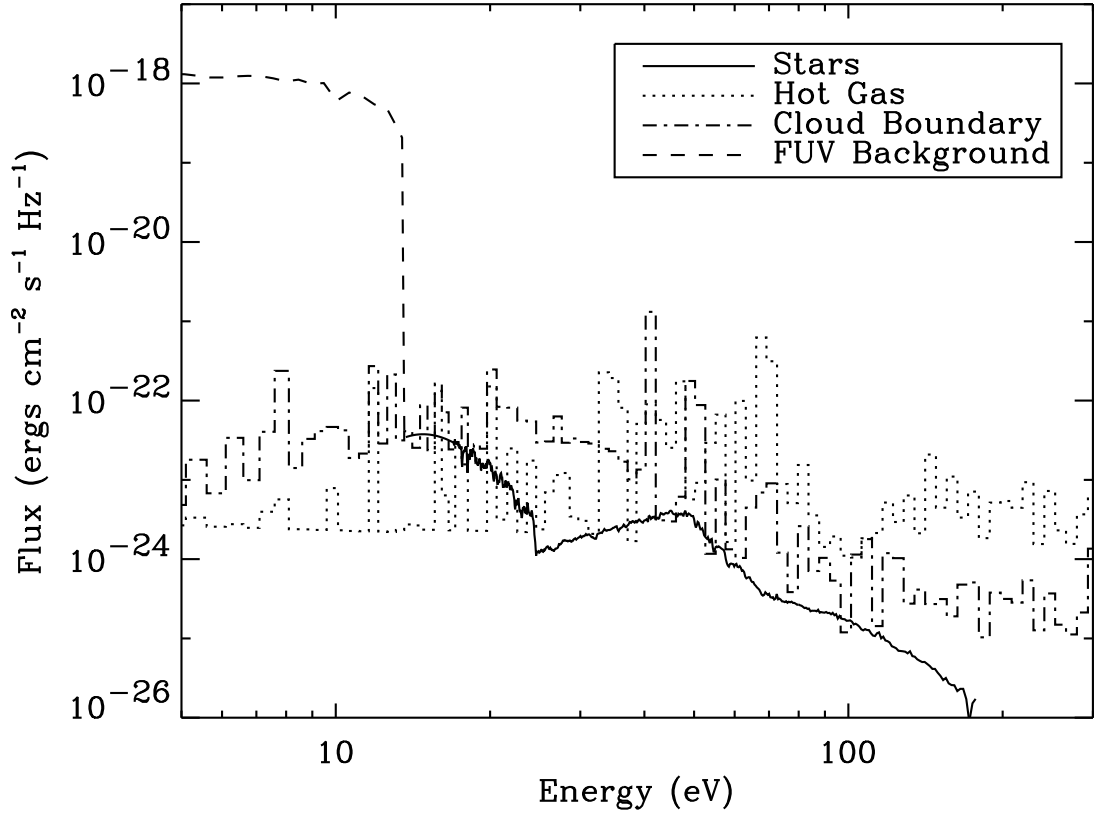


Fig. 1.— Model for the interstellar radiation field incident on the complex of local interstellar clouds (model no. 17). The FUV part is mostly from B stars (Gondhalekar et al. 1980). The curve labeled “Stars” is the EUV flux from nearby stars (WDs and B stars) observed by *EUVE* (Vallerga 1998), de-absorbed by an H I column density of $4 \times 10^{17} \text{ cm}^{-2}$ so as to get the flux incident from outside the cloud. The “Cloud Boundary” curve is the flux from an evaporative interface between the cloud and the hot gas of the Local Bubble. The “Hot Gas” part of the background is due to the $\log T = 6.1$ gas in the Local Bubble with the intensity scaled so that the hot gas + interface radiation is consistent with the all-sky average count rate in the soft X-rays measured in the Wisconsin B band (McCammon et al. 1983).

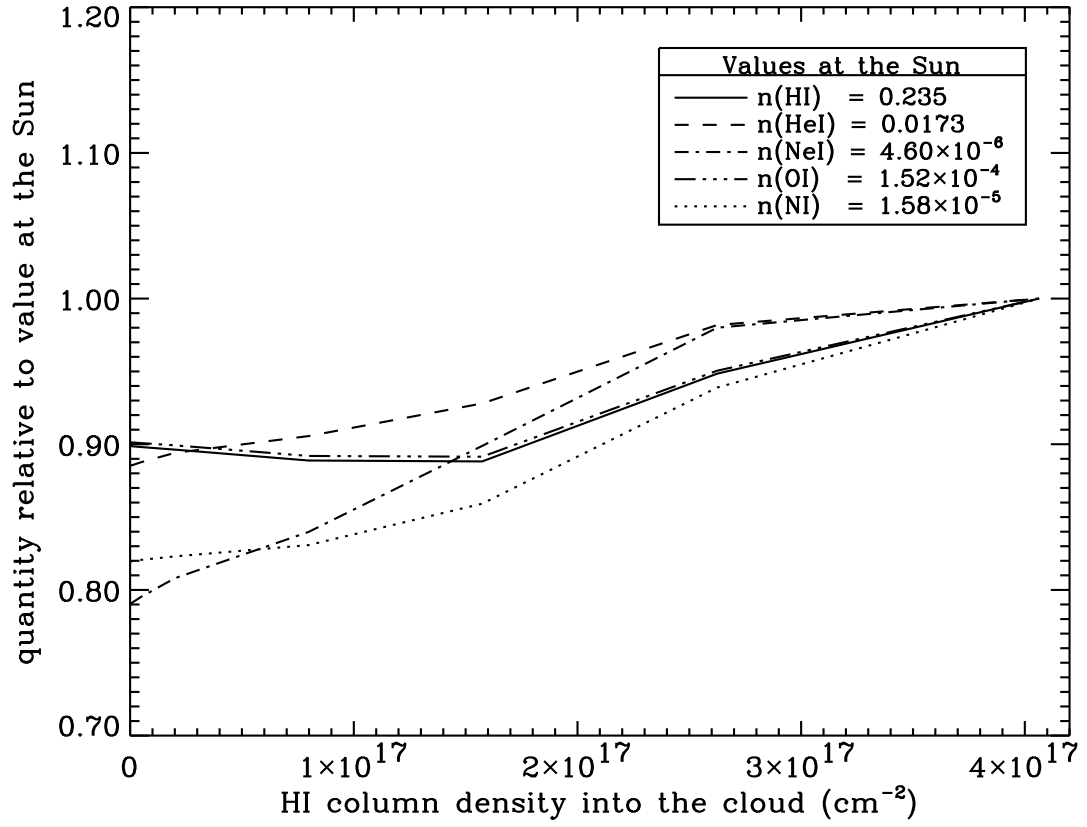


Fig. 2.— Densities of H I, He I, Ne I, O I, and N I relative to those at the Sun (for our model no. 17) as a function of depth (H I column density) into the cloud. The cloud surface is at the left and the solar location is at the right.

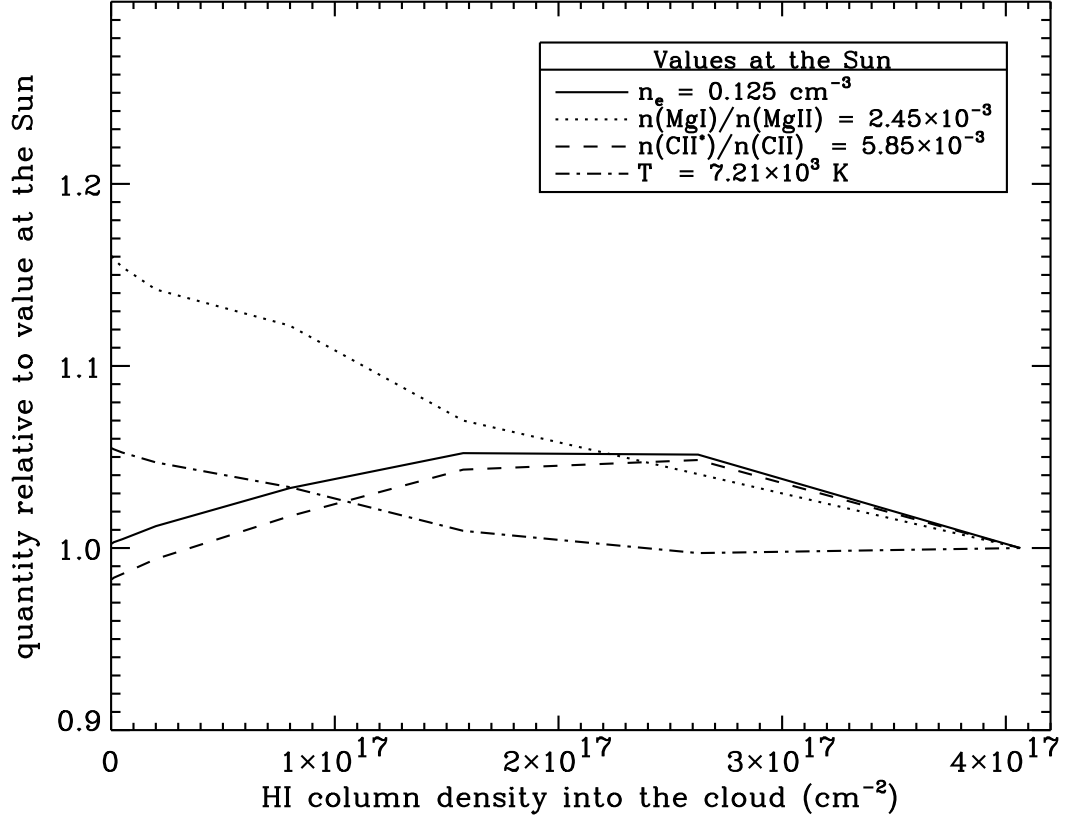


Fig. 3.— Measures of the electron density in the cloud and temperature (for our model no. 17) as a function of depth (H I column density) into the cloud. $n(\text{C II}^*)/n(\text{C II})$ can be seen to follow the true electron density closely while $n(\text{Mg I})/n(\text{Mg II})$ shows substantial deviation from n_e . The increase in n_e into the cloud is due to a combination of increasing trapping of diffuse Lyman continuum flux (leading to a slight increase in ionization) and an increase in total density to counter the temperature decrease and maintain constant pressure (see discussion in text).

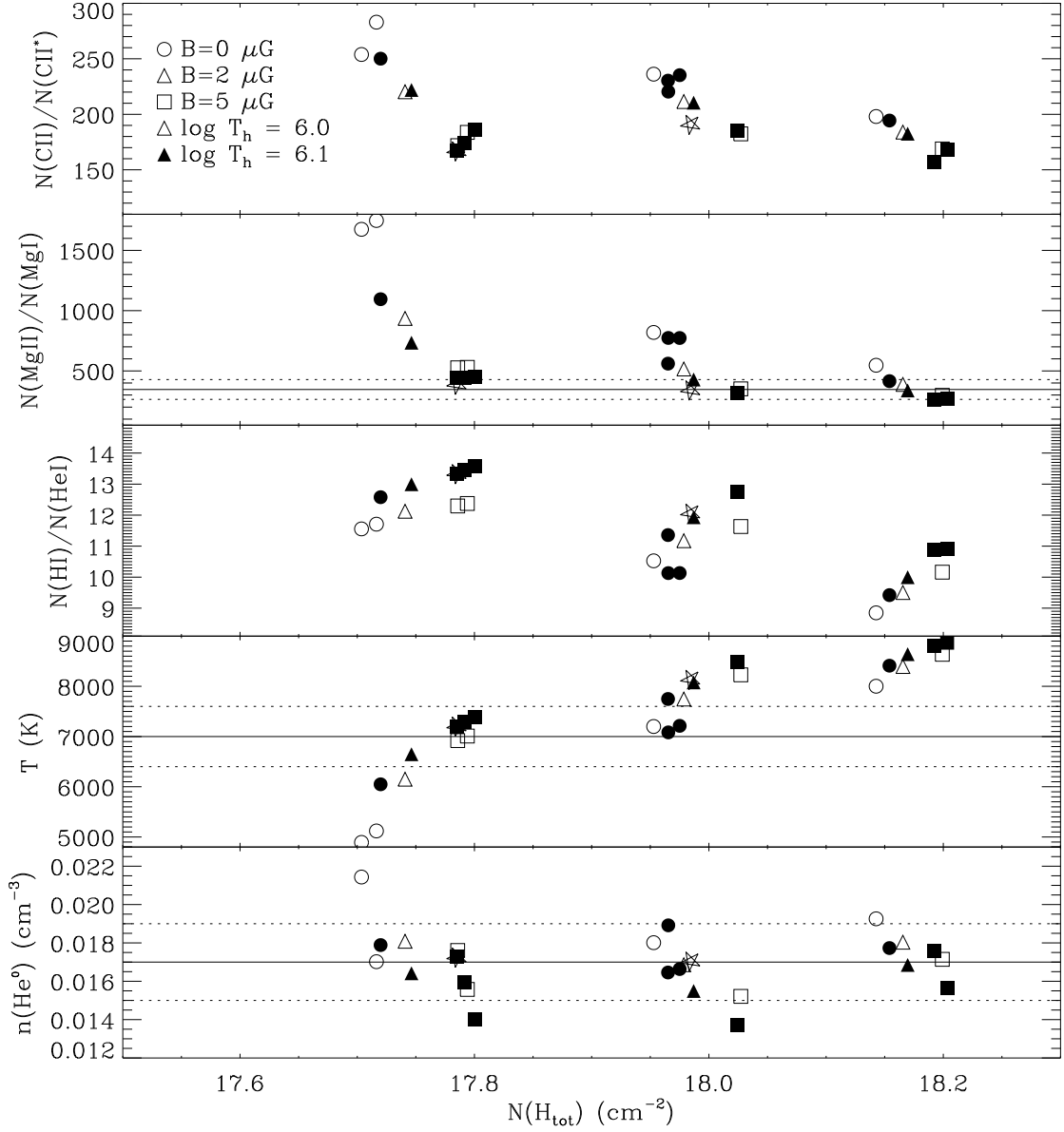


Fig. 4.— Model results for column density ratios $N(\text{C II})/N(\text{C II}^*)$, $N(\text{Mg II})/N(\text{Mg I})$, and $N(\text{H I})/N(\text{He I})$, and temperature and He^0 density at the solar location plotted against the total column density ($\text{H}^0 + \text{H}^+$). The three groups of $N(H_{\text{tot}})$ correspond to the three assumed values for $\log N(\text{H}^0) = 17.60, 17.81$, and 17.95 cm^{-2} . The observed value (and limits) for $N(\text{Mg II})/N(\text{Mg I})$ towards $\epsilon \text{ CMa}$, T , and $n(\text{He}^0)$ are denoted by solid (value) and dashed (limits) lines. The type of symbol denotes magnetic field strength in the model while filled/unfilled denotes the value of T_h . The starred symbols are for models with the Gondhalekar et al. (1980) FUV field (nos. 17 and 18) which are also the models which fit the data best. Note that cases in which the same symbol appears more than once in a grouping differ only in the assumed value of n_H .

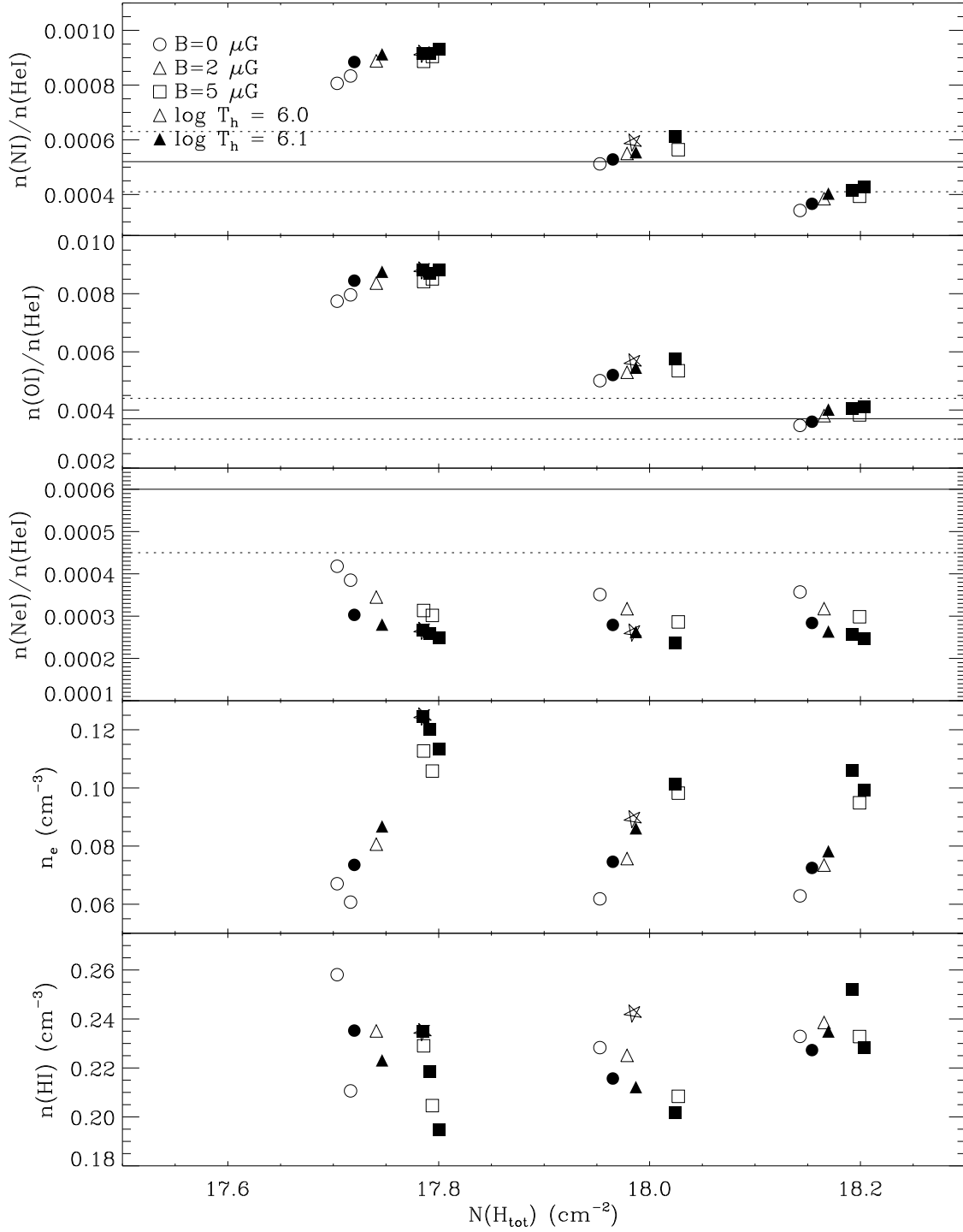


Fig. 5.— Model results in the same format as Figure 4. In this case we plot density ratios and densities for the solar location. The observed values (and limits) from PUI data are shown plotted as solid lines (dotted lines), from Table 1. The PUI data for O/He should be corrected upwards by $\sim 20\%$ for comparison with model predictions, to accomodate O filtration in the heliopause region (see text).

Table 1. Observational Constraints

Observed Quantity	Observed ^a Value	Reference
$N(\text{C II}) \text{ (cm}^{-2}\text{)}$	$2.1 - 3.4 \times 10^{14}$	1
$N(\text{C II}^*) \text{ (cm}^{-2}\text{)}$	$1.5 \pm 0.31 \times 10^{12}$	1
$N(\text{C IV})^{\text{b}} \text{ (cm}^{-2}\text{)}$	$1.2 \pm 0.3 \times 10^{12}$	1
$N(\text{N I}) \text{ (cm}^{-2}\text{)}$	$2.68 \pm 0.1 \times 10^{13}$	1
$N(\text{O I}) \text{ (cm}^{-2}\text{)}$	$2.6^{+0.8}_{-0.5} \times 10^{14}$	1
$N(\text{Mg I}) \text{ (cm}^{-2}\text{)}$	$1.2 \pm 0.3 \times 10^{10}$	1
$N(\text{Mg II}) \text{ (cm}^{-2}\text{)}$	$4.15 \pm 0.11 \times 10^{12}$	1
$N(\text{Si II}) \text{ (cm}^{-2}\text{)}$	$6.37 \pm 0.3 \times 10^{12}$	1
$N(\text{Si III}) \text{ (cm}^{-2}\text{)}$	$2.5 \pm 0.31 \times 10^{12}$	1
$N(\text{S II}) \text{ (cm}^{-2}\text{)}$	$1.35 \pm 0.36 \times 10^{13}$	1
$N(\text{Fe II}) \text{ (cm}^{-2}\text{)}$	$1.87 \pm 0.1 \times 10^{12}$	1
$N(\text{H I})/N(\text{He I})$	$14 \pm 0.4^{\text{c}}$	2
$n(\text{O I})/n(\text{N I})^{\text{d}}$	7.0 ± 1.5	3
$n(\text{O I})/n(\text{He I})^{\text{d}}$	$3.7 \pm 0.7 \times 10^{-3}$	3
$n(\text{N I})/n(\text{He I})^{\text{d}}$	$5.2 \pm 1.1 \times 10^{-4}$	3
$n(\text{Ne I})/n(\text{He I})^{\text{d}}$	$6.0 \pm 1.5 \times 10^{-4}$	3
$T(\text{K})^{\text{e}}$	7000 ± 600	4
$n(\text{He I}) \text{ (cm}^{-3}\text{)}$	0.017 ± 0.002	4

^a $N(\text{C II}^*)$, $N(\text{N I})$, $N(\text{O I})$, $N(\text{Mg II})$, $N(\text{Si II})$, $N(\text{S II})$ and $N(\text{Fe II})$ are used to constrain the input abundances of the models.

^bC IV is detected only in the LIC cloud.

^cThe uncertainty given is only that due to uncertainties listed in Dupuis et al. (1995) for the observed H I and He I column densities with the implicit assumption that the ratio is the same on all lines of sight. Given the substantial intrinsic variation in this ratio, however, the quoted uncertainty must be regarded as a lower limit to the true uncertainty.

^dNote that the pickup ion ratios are for values at the termination shock.

^eThe temperature shown represents the value derived from in-ecliptic He I data. An alternative Ulysses sample from north of the ecliptic yields a temperature of $6100 \pm 300 \text{ K}$ (Witte 1998, private communication).

References. — (1) Gry & Dupin (1998); Gry & Jenkins (2001) (Note that the values shown are for the LIC+BC combined towards $\epsilon \text{ CMa.}$), (2) Dupuis et al. (1995), (3) Gloeckler & Geiss (2001), Gloeckler, G., (2000, private communication), (4) Witte et al. (1996).

Table 2. Model Input Parameter Values

Model No.	Input Parameter Type				
	n_{H} (cm^{-3})	$\log T_h$	B_0 (μG) ^a	N_{HI} (10^{17} cm^{-2})	FUV field ^b
1	0.273	6.0	5.0	4.0	MMP
2	0.273	6.0	5.0	6.5	MMP
3	0.273	6.0	5.0	9.0	MMP
4	0.273	6.0	2.0	4.0	MMP
5	0.273	6.0	2.0	6.5	MMP
6	0.273	6.0	2.0	9.0	MMP
7	0.273	6.1	5.0	4.0	MMP
8	0.273	6.1	5.0	6.5	MMP
9	0.273	6.1	5.0	9.0	MMP
10	0.273	6.1	2.0	4.0	MMP
11	0.273	6.1	2.0	6.5	MMP
12	0.273	6.1	2.0	9.0	MMP
13	0.300	6.0	5.0	4.0	MMP
14	0.300	6.1	5.0	4.0	MMP
15	0.300	6.1	5.0	9.0	MMP
16	0.318	6.1	5.0	4.0	MMP
17	0.318	6.1	5.0	4.0	GPW
18	0.300	6.1	3.0	6.5	GPW
19	0.273	6.0	...	4.0	MMP
20	0.273	6.0	...	6.5	MMP
21	0.273	6.0	...	9.0	MMP
22	0.273	6.1	...	4.0	MMP
23	0.273	6.1	...	6.5	MMP
24	0.273	6.1	...	9.0	MMP
25	0.227	6.0	...	4.0	MMP

^aModels for which no magnetic field strength is given are those for which we have assumed that the cloud boundary is not conductive. For these models there is no evaporative boundary.

^bReference for FUV background field strength and shape. MMP is Mathis et al. (1983) and GPW Gondhalekar et al. (1980).

Table 3. Characteristics of the Model Radiation Field

Model	U	ϕ_{H}	ϕ_{He^0}	ϕ_{He^+}	$Q(\text{He}^0)/Q(\text{H}^0)$	$\langle E \rangle$
1	3.9×10^{-6}	9.2×10^3	1.6×10^4	5.6×10^3	0.49	57.8
2	4.2×10^{-6}	1.2×10^4	1.5×10^4	5.6×10^3	0.44	54.5
3	5.5×10^{-6}	2.3×10^4	1.5×10^4	5.6×10^3	0.33	44.8
4	2.6×10^{-6}	5.3×10^3	9.0×10^3	5.7×10^3	0.42	70.4
5	3.0×10^{-6}	8.5×10^3	8.9×10^3	5.7×10^3	0.36	63.3
6	4.4×10^{-6}	2.0×10^4	9.0×10^3	5.7×10^3	0.25	48.1
7	4.4×10^{-6}	8.1×10^3	1.8×10^4	8.4×10^3	0.50	59.9
8	4.6×10^{-6}	1.1×10^4	1.7×10^4	8.3×10^3	0.45	56.7
9	6.0×10^{-6}	2.2×10^4	1.7×10^4	8.3×10^3	0.34	47.3
10	3.0×10^{-6}	5.1×10^3	1.0×10^4	8.5×10^3	0.40	70.9
11	3.4×10^{-6}	8.4×10^3	9.8×10^3	8.5×10^3	0.35	64.7
12	4.8×10^{-6}	2.0×10^4	9.9×10^3	8.4×10^3	0.25	50.5
13	3.6×10^{-6}	9.2×10^3	1.6×10^4	5.5×10^3	0.50	57.7
14	4.0×10^{-6}	8.2×10^3	1.8×10^4	8.3×10^3	0.50	59.7
15	5.5×10^{-6}	2.3×10^4	1.7×10^4	8.2×10^3	0.35	47.2
16	3.8×10^{-6}	9.8×10^3	1.8×10^4	3.5×10^3	0.54	60.6
17	3.8×10^{-6}	9.8×10^3	1.8×10^4	3.5×10^3	0.54	60.6
18	3.4×10^{-6}	1.0×10^4	1.2×10^4	3.5×10^3	0.43	63.9
19	1.9×10^{-6}	3.6×10^3	4.9×10^3	5.8×10^3	0.32	83.4
20	2.3×10^{-6}	7.0×10^3	4.8×10^3	5.7×10^3	0.25	71.9
21	3.6×10^{-6}	1.8×10^4	4.7×10^3	5.7×10^3	0.16	50.8
22	2.4×10^{-6}	3.7×10^3	6.3×10^3	8.6×10^3	0.31	79.7
23	2.8×10^{-6}	7.0×10^3	6.1×10^3	8.6×10^3	0.26	71.0
24	4.1×10^{-6}	1.8×10^4	6.0×10^3	8.5×10^3	0.17	52.9
25	2.3×10^{-6}	3.6×10^3	4.9×10^3	5.8×10^3	0.32	83.4

Table 4. Model Column Density Results

Model	$\log N(\text{H}_{\text{tot}})$	$\log N(\text{Ar I})$	$\log N(\text{Ar II})$	$\log N(\text{Si III})$	$\frac{N(\text{Mg II})}{N(\text{Mg I})}$	$\frac{N(\text{C II})}{N(\text{C II}^*)}$	$\frac{N(\text{H I})}{N(\text{He I})}$
Obs. ^a	12.40	346 ± 82	110 – 280	12 – 16
1	17.79	11.44	11.96	10.20	529.3	183.7	12.38
2	18.03	11.71	12.19	10.49	351.0	182.4	11.63
3	18.20	11.93	12.38	10.63	297.3	168.8	10.16
4	17.74	11.55	11.91	9.77	935.2	220.3	12.12
5	17.98	11.81	12.15	10.22	515.8	211.5	11.17
6	18.17	12.02	12.35	10.45	388.0	184.0	9.51
7	17.80	11.42	11.94	10.31	447.4	185.9	13.59
8	18.02	11.69	12.17	10.53	316.4	185.4	12.74
9	18.20	11.91	12.36	10.68	270.9	167.8	10.90
10	17.75	11.52	11.90	9.95	734.2	221.9	13.00
11	17.99	11.78	12.14	10.33	428.7	210.5	11.93
12	18.17	11.99	12.34	10.53	337.9	182.6	10.00
13	17.79	11.46	11.95	10.15	525.8	171.8	12.29
14	17.79	11.44	11.94	10.26	441.2	174.2	13.44
15	18.19	11.92	12.36	10.64	264.3	157.2	10.90
16	17.79	11.45	11.93	10.23	441.9	167.0	13.34
17	17.79	11.45	11.93	10.23	389.2	167.0	13.34
18	17.98	11.77	12.14	10.34	341.9	190.9	12.06
19	17.70	11.64	11.87	9.08	1675	253.9	11.56
20	17.95	11.89	12.12	9.92	819.3	236.2	10.53
21	18.14	12.10	12.32	10.22	546.9	198.0	8.85
22	17.72	11.58	11.87	9.64	1095	250.1	12.58
23	17.97	11.85	12.12	10.16	560.6	230.3	11.36
24	18.15	12.06	12.33	10.39	415.3	194.4	9.42
25	17.72	11.61	11.88	9.24	1748	283.0	11.71

^aObservational results from Gry & Jenkins (2001) (see table 1). The values listed for $N(\text{H I})/N(\text{He I})$ are the range of values observed excluding Feige 24 which is one of the most distant stars observed by Dupuis et al. (1995) and has unusually large $N(\text{H I})$ and ratio values.

Table 5. High Ion Column Densities For Models Including Cloud Evaporation ^a

Model	$\log N(\text{C IV})$	$\log N(\text{N V})$	$\log N(\text{O VI})$	$\log N(\text{Si IV})$	$\log N(\text{Si III})$
1	12.35	11.89	13.03	10.27	10.12
2	12.11	11.68	12.81	10.05	9.90
3	11.92	11.53	12.68	9.90	9.77
4	12.38	11.72	12.84	10.25	10.00
5	12.13	11.53	12.64	10.04	9.79
6	11.91	11.39	12.52	9.88	9.64
7	12.32	11.86	12.95	10.26	10.03
8	12.10	11.66	12.74	10.04	9.81
9	11.89	11.51	12.60	9.88	9.66
10	12.35	11.65	12.72	10.23	9.98
11	12.09	11.46	12.52	10.00	9.75
12	11.87	11.33	12.40	9.86	9.62
13	12.32	11.88	13.03	10.28	10.13
14	12.30	11.85	12.95	10.25	10.03
15	11.87	11.50	12.61	9.88	9.67
16	12.29	11.85	12.96	10.27	10.04
17	12.29	11.85	12.96	10.27	10.04
18	12.10	11.54	12.61	10.03	9.74

^aNote that the rows for models 16 and 17 are identical since the same values for the parameters that affect cloud evaporation (n_{cl} , T_h , B_0 and $N(\text{H I})$), were used. The difference between the models in this case is the different FUV radiation fields used. The difference in the FUV field has negligible effect on the column densities of the high ions.

Table 6. Elemental Gas Phase Abundances (ppm)

Model No.	Element						
	C	N	O	Mg	Si	S	Fe
1	457	81.3	631	7.94	10.2	22.4	3.16
2	263	50.1	380	4.68	6.03	13.2	1.86
3	166	34.7	275	3.09	4.07	8.91	1.26
4	617	74.1	631	9.12	11.5	25.1	3.55
5	339	46.8	389	5.25	6.76	14.5	2.04
6	191	33.1	282	3.39	4.37	9.55	1.35
7	457	83.2	617	8.13	10.2	22.4	3.09
8	275	52.5	380	4.90	6.03	13.2	1.86
9	162	36.3	275	3.16	3.98	8.71	1.26
10	617	75.9	631	9.33	11.5	25.1	3.47
11	331	47.9	389	5.37	6.61	14.5	2.00
12	191	33.9	282	3.47	4.37	9.33	1.35
13	437	79.4	631	7.94	10.5	22.9	3.24
14	437	81.3	617	8.13	10.2	22.9	3.16
15	155	35.5	275	3.24	4.07	8.91	1.29
16	427	81.3	631	8.32	10.5	23.4	3.24
17	427	81.3	631	8.32	10.5	23.4	3.24
18	309	49.0	389	5.37	6.61	14.5	2.04
19	759	67.6	631	9.77	12.6	27.5	3.80
20	398	43.7	389	5.62	7.08	15.5	2.14
21	219	30.9	282	3.55	4.57	10.0	1.41
22	724	72.4	631	10.0	12.0	26.9	3.63
23	380	45.7	389	5.75	6.92	15.1	2.09
24	209	32.4	275	3.63	4.47	9.77	1.38
25	832	69.2	631	9.77	12.3	26.9	3.72

Table 7. Model Results for Solar Location

Model	$X(\text{H})$	$X(\text{He})$	O I/N I	O I/He I	N I/He I	Ne I/He I	Ar I/Ar _{tot}	T	$n(\text{H I})$	$n(\text{He I})$	n_e
Obs. ^a	7.0	3.7×10^{-3}	5.2×10^{-4}	6.0×10^{-4}	...	7000	...	0.017	...
1	0.309	0.467	9.41	8.51×10^{-3}	9.05×10^{-4}	3.02×10^{-4}	0.180	7010	0.205	0.0156	0.106
2	0.287	0.471	9.49	5.35×10^{-3}	5.64×10^{-4}	2.86×10^{-4}	0.199	8230	0.208	0.0152	0.0982
3	0.256	0.444	9.73	3.83×10^{-3}	3.93×10^{-4}	2.98×10^{-4}	0.235	8640	0.233	0.0171	0.0949
4	0.224	0.396	9.41	8.36×10^{-3}	8.88×10^{-4}	3.45×10^{-4}	0.253	6150	0.235	0.0181	0.0806
5	0.221	0.408	9.64	5.30×10^{-3}	5.50×10^{-4}	3.18×10^{-4}	0.263	7750	0.225	0.0169	0.0757
6	0.204	0.389	9.89	3.80×10^{-3}	3.85×10^{-4}	3.18×10^{-4}	0.296	8400	0.239	0.0180	0.0735
7	0.332	0.507	9.45	8.81×10^{-3}	9.32×10^{-4}	2.48×10^{-4}	0.164	7380	0.195	0.0140	0.113
8	0.300	0.511	9.42	5.76×10^{-3}	6.12×10^{-4}	2.37×10^{-4}	0.182	8480	0.202	0.0137	0.101
9	0.266	0.483	9.66	4.12×10^{-3}	4.27×10^{-4}	2.47×10^{-4}	0.216	8870	0.228	0.0156	0.0993
10	0.245	0.432	9.59	8.76×10^{-3}	9.13×10^{-4}	2.80×10^{-4}	0.229	6650	0.223	0.0164	0.0868
11	0.255	0.442	9.84	5.45×10^{-3}	5.54×10^{-4}	2.63×10^{-4}	0.233	8080	0.212	0.0155	0.0861
12	0.215	0.423	9.96	4.02×10^{-3}	4.03×10^{-4}	2.64×10^{-4}	0.272	8640	0.235	0.0169	0.0782
13	0.298	0.454	9.50	8.42×10^{-3}	8.87×10^{-4}	3.13×10^{-4}	0.190	6920	0.229	0.0176	0.113
14	0.319	0.493	9.51	8.70×10^{-3}	9.15×10^{-4}	2.59×10^{-4}	0.174	7290	0.219	0.0159	0.120
15	0.259	0.472	9.75	4.05×10^{-3}	4.16×10^{-4}	2.58×10^{-4}	0.226	8810	0.252	0.0176	0.106
16	0.312	0.484	9.63	8.82×10^{-3}	9.16×10^{-4}	2.66×10^{-4}	0.180	7210	0.235	0.0173	0.125
17	0.312	0.484	9.63	8.82×10^{-3}	9.16×10^{-4}	2.66×10^{-4}	0.180	7210	0.235	0.0173	0.125
18	0.234	0.448	9.56	5.65×10^{-3}	5.91×10^{-4}	2.62×10^{-4}	0.240	8140	0.242	0.0170	0.0894
19	0.180	0.313	9.60	7.74×10^{-3}	8.06×10^{-4}	4.18×10^{-4}	0.322	4890	0.258	0.0214	0.0671
20	0.183	0.346	9.78	5.01×10^{-3}	5.12×10^{-4}	3.51×10^{-4}	0.321	7200	0.228	0.0180	0.0618
21	0.186	0.319	10.2	3.47×10^{-3}	3.42×10^{-4}	3.57×10^{-4}	0.350	8000	0.233	0.0193	0.0629
22	0.207	0.385	9.55	8.45×10^{-3}	8.84×10^{-4}	3.03×10^{-4}	0.274	6050	0.235	0.0179	0.0735
23	0.226	0.395	9.85	5.20×10^{-3}	5.28×10^{-4}	2.79×10^{-4}	0.274	7750	0.216	0.0165	0.0746
24	0.211	0.371	9.83	3.60×10^{-3}	3.66×10^{-4}	2.84×10^{-4}	0.307	8410	0.227	0.0177	0.0725
25	0.194	0.341	9.55	7.96×10^{-3}	8.33×10^{-4}	3.85×10^{-4}	0.295	5120	0.211	0.0170	0.0607

^aObservational results from Gloeckler & Geiss (2001), Gloeckler (2000) and Witte et al. (1996) (see table 1 for uncertainties).

Table 8. Model Predictions for Ionization Fractions at the Sun ^a

Element	Abundance (ppm)	Ionization Fraction			
		I	II	III	IV
H	10 ⁶	0.688	0.312
He	10 ⁵	0.506	0.484	0.0103	...
C	427	0.0005	0.964	0.0352	0.0
N	81.3	0.570	0.430	0.0003	0.0
O	631	0.707	0.293	0.0001	0.0
Ne	123	0.110	0.627	0.264	0.0
Na	2.04	0.0028	0.865	0.132	0.0
Mg	8.32	0.0020	0.827	0.171	0.0
Al	0.0794	0.0001	0.973	0.0204	0.0066
Si	10.5	0.0	0.998	0.0022	0.0
P	0.219	0.0002	0.968	0.0314	0.0001
S	23.4	0.0001	0.959	0.0413	0.0
Ar	2.82	0.180	0.493	0.328	0.0
Ca	0.000407	0.0	0.0247	0.975	0.0003
Fe	3.24	0.0002	0.962	0.0378	0.0

^aResults for model no. 17 as described in Table 2.